

# **IDEA League**

MASTER OF SCIENCE IN APPLIED GEOPHYSICS  
RESEARCH THESIS

---

## **Seismic deblending of crossline sources**

**Christian Reinicke Urruticoechea**

---

August 3, 2015



# **Seismic deblending of crossline sources**

MASTER OF SCIENCE THESIS

for the degree of Master of Science in Applied Geophysics at  
Delft University of Technology  
ETH Zürich  
RWTH Aachen University  
by

Christian Reinicke Urruticoechea

August 3, 2015

Department of Geoscience & Engineering	.	Delft University of Technology
Department of Earth Sciences	.	ETH Zürich
Faculty of Georesources and Material Engineering	.	RWTH Aachen University



**Delft University of Technology**

Copyright © 2013 by IDEA League Joint Master's in Applied Geophysics:

Delft University of Technology, ETH Zürich, RWTH Aachen University

All rights reserved.

No part of the material protected by this copyright notice may be reproduced or utilized in any form or by any means, electronic or mechanical, including photocopying or by any information storage and retrieval system, without permission from this publisher.

Printed in The Netherlands, Switzerland, Germany

IDEA LEAGUE  
JOINT MASTER'S IN APPLIED GEOPHYSICS

Delft University of Technology, The Netherlands  
ETH Zürich, Switzerland  
RWTH Aachen, Germany

Dated: *August 3, 2015*

Supervisor(s): Dr. Ir. G.J.A. van Groenestijn

Dr. Ir. G.G.Drijkoningen

Committee Members: Dr. Ir. G.J.A. van Groenestijn

Dr. Ir. G.G.Drijkoningen

Dr. M. Hruska



---

# Abstract

Blending is a recent seismic acquisition design which allows seismic shots to interfere. Blending is beneficial in terms of data quality and acquisition costs. Current processing techniques are not capable to deal with blended data. Consequently, the blended data must be separated as if they were acquired in a conventional way. The separation technique is referred to as deblending.

This thesis reviews the 2D deblending method of [Mahdad et al. \(2011\)](#), which is a noise prediction and subtraction method. Thus, it is demonstrated how deblending benefits from incoherent shot interference, so-called blending noise. In this context a new measure of incoherency is introduced, and 3 possibilities of incoherent blending are proposed. The effect of incoherency on the deblending quality is analyzed at the example of 2D synthetic data. The results suggest that optimal deblending quality is achieved by maximizing the incoherency of the blended acquisition.

Based on the 2D method of [Mahdad et al. \(2011\)](#) a 3D deblending method is derived. The key differences between the 2D and 3D methods are; (1) the data sorting, and (2) the coherency filter. Next, the presented method is tested on a complex synthetic data set. The results demonstrate that the method successfully deblends strong interfering events. The deblending of weak late events is not optimal yet.

In total, the results indicate that 3D crossline blending is a potential acquisition design. With some further development 3D crossline blending is promising to become feasible as a standard acquisition design.



---

# Table of Contents

<b>Abstract</b>	<b>v</b>
<b>1 Introduction</b>	<b>1</b>
1-1 Marine Seismic Acquisition . . . . .	1
1-2 Literature Review . . . . .	2
1-3 New Survey Design: Crossline Blending (3D) . . . . .	3
1-4 Thesis Outline . . . . .	5
<b>2 2D Blending and Deblending</b>	<b>7</b>
2-1 The Forward Model of Blending . . . . .	7
2-1-1 Conventional Seismic Data . . . . .	7
2-1-2 Blended Seismic Data . . . . .	9
2-2 Deblending . . . . .	10
2-2-1 Pseudo-Deblending . . . . .	10
2-2-2 Common-Receiver Gather . . . . .	11
2-2-3 Iterative Estimation of Blending Noise . . . . .	11
<b>3 Incoherency</b>	<b>17</b>
3-1 Analysis of the Blending Matrix . . . . .	17
3-2 Results Spatial and Temporal Incoherency . . . . .	20
3-3 Effect of Incoherency . . . . .	21
3-4 Results Incoherency . . . . .	23
3-5 Effect of Maximum Firing-Time Delay . . . . .	24
3-6 Results Maximum Firing-Time Delay . . . . .	24
3-7 Conclusions . . . . .	25

<b>4 Crossline Deblending (3D)</b>	<b>27</b>
4-1 Data Sorting . . . . .	27
4-2 3D $f-k_x-k_y$ Filter . . . . .	30
4-3 Results . . . . .	30
4-4 Conclusions . . . . .	35
<b>5 Results Complex Synthetic Data</b>	<b>37</b>
5-1 Large Crossline Source Array . . . . .	37
5-2 Dense Crossline Source Array . . . . .	42
5-3 Conclusion and Discussion . . . . .	46
<b>6 Conclusions and Discussion</b>	<b>47</b>
6-1 Conclusions . . . . .	47
6-2 Discussion . . . . .	47
<b>Acknowledgements</b>	<b>49</b>
<b>Bibliography</b>	<b>51</b>
<b>A The back of the thesis</b>	<b>53</b>
A-1 An appendix section . . . . .	53
A-1-1 An appendix subsection with C++ Listing . . . . .	53
A-1-2 A MATLAB Listing . . . . .	53

---

# Nomenclature

## Abbreviations

$\Delta t_{ij}$	Time delay of the $i^{th}$ source in the $j^{th}$ experiment
$\gamma_{ij}$	Element of the blending matrix $\Gamma$ corresponding to the $i^{th}$ source and the $j^{th}$ experiment
$\Gamma$	(Monochromatic) blending matrix as a function of source and experiment number
$\Gamma^H$	(Monochromatic) conjugate transpose of the blending matrix $\Gamma$ as a function of experiment and source number
$\Gamma_{coh}$	(Monochromatic) blending matrix with constant firing-time delays
$\Gamma_{eff}$	Linear superposition of the blending matrices $\Gamma_{coh}$ and $\Gamma_{ran}$
$\Gamma_{ran}$	(Monochromatic) blending matrix with random firing-time delays
$\mathbf{D}$	(Monochromatic) receiver matrix as a function of receiver number
$\mathbf{I}$	Identity matrix
$\mathbf{N}$	(Monochromatic) blending noise matrix as a function of receiver and source number
$\mathbf{P}$	(Monochromatic) data matrix as a function of receiver and source number
$\mathbf{p}$	3D data cube as a function of time, receiver coordinates, and source coordinates
$\mathbf{P}_{bl}$	(Monochromatic) blended data matrix as a function of receiver and experiment number
$\mathbf{P}_{ps}$	(Monochromatic) pseudo-deblended data matrix as a function of receiver and source number
$\mathbf{S}$	(Monochromatic) source matrix as a function of source number
$\mathbf{S}_{bl}$	(Monochromatic) blended source matrix as a function of source and experiment number
$\mathbf{X}$	(Monochromatic) earth impulse response matrix as a function of receiver and source number
$\mu$	Incoherency value of the blending matrix $\Gamma$
$\mu_{coh}$	Incoherency of the blending matrix $\Gamma_{coh}$
$\mu_{ran}$	Incoherency of the blending matrix $\Gamma_{ran}$

---

$\omega$	Circular frequency
$\bar{\mathbf{P}}$	(Monochromatic) data matrix after thresholding as a function of receiver and source number
$\hat{\mathbf{P}}_i$	(Monochromatic) data matrix prediction after $i$ iterations as a function of receiver and source number
$\hat{\mathbf{N}}_i$	(Monochromatic) blending noise prediction after $i$ iterations as a function of receiver and source number
$A_{ij}$	Amplitude of the element $\gamma_{ij}$ of the blending matrix $\mathbf{\Gamma}$
$f$	Frequency
$f_{cut}$	High cut frequency of the $f$ - $k$ mask
$g_{ij}$	Element of the matrix product $\mathbf{\Gamma}\mathbf{\Gamma}^H$ corresponding to the interference between the $i^{th}$ and $j^{th}$ source
$k$	Wavenumber in a 2D case
$k_T$	Total wavenumber
$k_x$	Crossline wavenumber in a 3D case
$k_y$	Inline wavenumber in a 3D case
$k_{max}$	Maximum wavenumber for a given frequency $f$
$M(d, \omega)$	(Monochromatic) absolute value of the sum along the $d^{th}$ sub-diagonal of the matrix product $\mathbf{\Gamma}\mathbf{\Gamma}^H(\omega)$
$N_s$	Total number of sources
$Ns_x$	Number of sources in crossline direction
$Ns_y$	Number of sources in inline direction
$Q$	Quality factor
$s_{ii}$	Diagonal element of the source matrix $\mathbf{S}$
$t$	Time
$v_w$	Seismic velocity in water
$v_{min}$	Minimum wavefield velocity present in the subsurface
$x$	Crossline space coordinate
$x_i$	Coordinates of the $i^{th}$ source
$x_r$	Receiver coordinates
$x_s$	Source coordinates
$y$	Inline space coordinate
CDP	Common-depth point
CRG	Common-receiver gather
CSG	Common-shot gather

---

# Chapter 1

---

## Introduction

Blended acquisition can be illustrated with the graduate problem. Each year students of the Idea League apply for final thesis projects. On a specific day representatives of several companies travel to Aachen university to present their projects and to interview the students. Among them is a Norwegian seismic service company. Unfortunately, the manager has not enough time to interview each candidate individually. Therefore, he invites all candidates at the same time and asks them to answer to his questions simultaneously. He records their answers with his phone. Obviously, the recording is not understandable at all because the answers are interfered or "blended". Luckily, the manager has a smart deblending algorithm, which is capable to separate, or "deblend", the recording into multiple recordings, as if the answer of each student was recorded separately. These recordings are clearly understandable and the manager can pick the ideal candidate.

This thesis solves a similar problem, where interfered (blended) seismic sources are recorded and separated (deblended) instead of students.

### 1-1 Marine Seismic Acquisition

Today, fossil energy accounts for about 80 % of the total primary energy supply, based on the World Energy Council ([WEC, 2013](#)). It is expected that in 2020 76 % of the total primary energy supply are still covered by fossil energy. However, the required fossil energy sources are not discovered yet. Thus, society depends on the exploration of new hydrocarbon reservoirs.

A standard method for hydrocarbon exploration is seismic acquisition, which images the subsurface with acoustic waves. The acquisition design has a significant impact on the data quality, and thus, on the success of the exploration. As a substantial part of the remaining hydrocarbon reserves is deposited in complex geologies, it is crucial to continuously optimize seismic acquisition techniques, i.e. increase data quality and lower acquisition costs. In view of these challenges this thesis proposes a new acquisition design; "3D crossline blending".

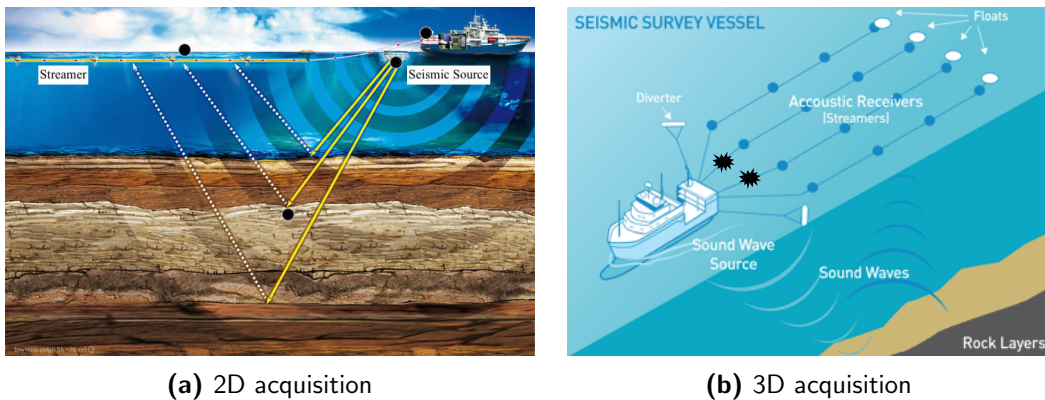


**Figure 1-1:** Illustration of (a) 2D and (b) 3D marine seismic acquisition. Both pictures are taken from the website [Wikigrewal \(2015\)](#).

## Conventional Acquisition

In a conventional marine acquisition set-up a vessel tows one source (2D acquisition) or two sources (3D acquisition), i.e. airguns, and multiple receivers, i.e. hydrophones. The receivers are located on, either a single streamer (2D acquisition), or on several streamers (3D acquisition). Figure 1-1 illustrates the conventional 2D and 3D acquisition set-up. The seismic source emits an acoustic wavefield, which is reflected in the subsurface and detected by the receivers.

Acquisition tries to find a balance between costs and quality. The major acquisition costs are defined by the survey time. The data quality depends on the number and density of shots and receivers. During conventional acquisition successive shots must be separated by sufficient time to avoid shot interference. This time increases the survey duration, and the seismic vessel moves during this time causing the spatial source sampling to be coarse. Hence, the time between successive shots is unfavorable for both acquisition costs and data quality.

## Blended Acquisition

In blended acquisition, or simultaneous source acquisition, the recorded events of seismic shots may interfere. The two major advantages are; (1) illumination of the subsurface from multiple angles to improve the spatial source sampling, and (2) reduction of the survey duration due to shorter times between successive shots. When designing a blended acquisition one can decide to put more weight on enhancing the data quality, or on reducing the survey duration.

Existing blended acquisition designs blend sources along the inline direction (2D blending). As current processing techniques cannot deal with blended data the data must be deblended, i.e. the interfering shots are separated as if they were recorded in a conventional fashion.

## 1-2 Literature Review

The success of seismic deblending strongly depends on the acquisition design. In case of land data blended sources can be encoded by applying different sweeps and polarities, thus,

the deblending problem can be controlled (Womack et al., 1990). Wu (2014) demonstrated that in marine acquisition impulsive sources can be coded and decoded as well.

Beasley et al. (1998) first proposed to apply simultaneous sources without source encoding. His method relies on a significant spatial separation of the blended shots. He separated the blended shots via normal moveout discrimination.

Vaage (2002) suggested a blended acquisition design with random firing-time delays. The set-up consists of two seismic sources, which are towed at a fixed distance. In each experiment the two sources are fired with a time delay, which differs for each blended experiment. Consequently, the recorded events of the second source become incoherent in any domain but the common-shot domain, allowing it to be separated with a coherency constraint.

This thesis builds further on the 2D deblending method of Mahdad et al. (2011), which uses both a coherency constraint in the frequency-wavenumber domain and a sparsity constraint in the space-time domain in their inversion method to deblend. Others like Ibrahim and Sacchi (2013) have also used this method to build on. They apply their constraints in the Radon domain.

## 1-3 New Survey Design: Crossline Blending (3D)

Existing blended acquisition designs blend 2 sources per experiment. Due to the movement of the vessel the blended shots are located on a line, i.e. the blending is 2D. This thesis proposes a new survey design, 3D crossline blending, which blends 7 crossline sources per experiment. The vessel moves such that the firing-positions of the blended shots are distributed on a 2D area. Thus, by including time the crossline blending is a 3D process.

Figure 1-2, 1-3 and 1-4 show a conventional 3D acquisition design and 2 acquisition designs with blended crossline sources.

### Conventional 3D Acquisition (see Figure 1-2)

The two sources are fired with sufficient time delay to avoid interference of the recorded events. In this set-up multiple receiver cables are applied. The source crossline-spacing determines the width of the individual bins. The receiver cables determine the inline and crossline widths of the acquired area indicated in gray.

### Large Crossline Source Array (see Figure 1-3)

The crossline is covered by a source cable and the inline is covered by a single receiver cable. The set-up acquires the same area as the conventional one, but it avoids cable tangling and facilitates faster turn arounds of the vessel. This thesis will examine the feasibility of this set-up as it illustrates the possibility to reduce the acquisition costs.

### Dense Crossline Source Array (see Figure 1-4)

The crossline sources are densely spaced in order to reduce the width of the individual bins. Thus, the data quality is enhanced in terms of angle diversity and resolution. By using multiple receiver cables the acquired area is maintained. This thesis will analyze how significantly this set-up enhances the data quality.

The acquisition designs in Figure 1-3 and 1-4 rely on heavily blended data in the order of 7 shots per experiment. Current 2D deblending methods are not capable to deblend this.

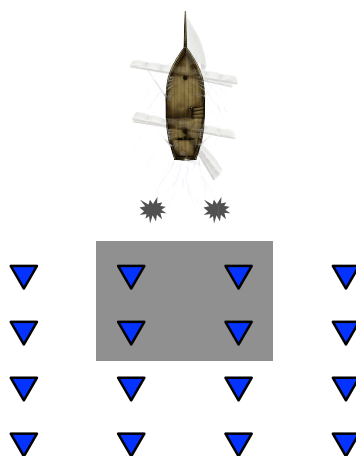


**Figure 1-2:** Conventional 3D marine acquisition design. The seismic sources are indicated in gray, and the receivers in blue. The gray rectangle illustrates the acquired area.

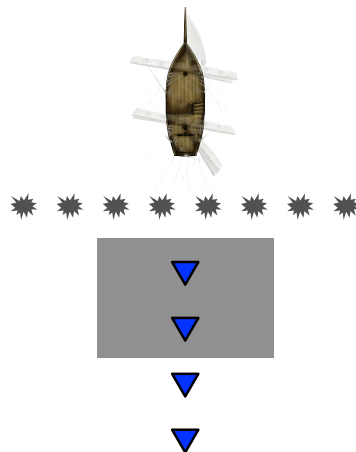


**Figure 1-3:** Large Crossline Source Array. The seismic sources are indicated in gray, and the receivers in blue. The gray rectangle illustrates the acquired area.

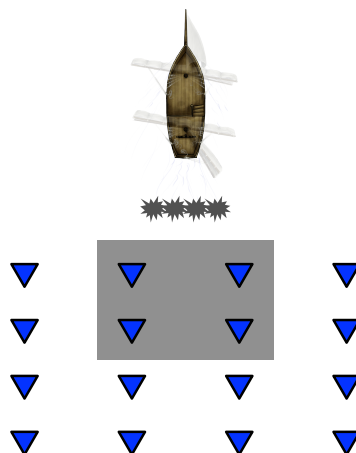


**Figure 1-4:** Dense Crossline Source Array. The seismic sources are indicated in gray, and the receivers in blue. The gray rectangle illustrates the acquired area.

Therefore, I will present a way to improve the blending design by increasing incoherency and introduce 3D deblending.

## 1-4 Thesis Outline

The content of the thesis is outlined below.

### **Chapter 2: 2D Blending and Deblending**

In this chapter the forward model of conventional and blended seismic data is explained. Next, the deblending method of [Mahdad et al. \(2011\)](#) is discussed in detail.

### **Chapter 3: Incoherency**

The effect of an incoherent blending pattern on the deblending quality is analyzed. In particular, the properties of so-called temporal and spatial incoherent blending are discussed. For this purpose I will introduce a new measure of incoherency. I will demonstrate that the deblending result is enhanced by maximizing the incoherency of the blended sources.

### **Chapter 4: Crossline Deblending (3D)**

I will derive a 3D deblending method based on coherency and sparsity constraints. In particular, the data sorting and the design of a 3D  $f-k_x-k_y$  filter are discussed.

### **Chapter 5: Results Complex Synthetic Data**

In this chapter I will apply the outcomes of chapter 3 and 4 to deblend complex synthetic data, which are acquired with the configurations of Figure 1-3 and 1-4.

### **Chapter 6: Conclusions and Discussion**

The main conclusions of the thesis are summarized and discussed.



---

# Chapter 2

---

## 2D Blending and Deblending

This chapter recapitulates the idea behind blending and deblending. First the detail hiding operator notation is explained. This notation is used to describe the forward model of seismic data. By introducing the blending operator the forward model is extended to the blended case. Next, the deblending method presented in [Mahdad et al. \(2011\)](#) is discussed to illustrate some of the concepts used in this thesis.

### 2-1 The Forward Model of Blending

#### 2-1-1 Conventional Seismic Data

In the detail hiding operator notation ([Berkhout, 1982](#)) the recorded signal is considered discrete in terms of time  $t$ , receiver position  $x_r$ , and source position  $x_s$ . Thus, the measurements can be organized in a cube,  $\mathbf{p}(t, x_r, x_s)$ , (see Figure 2-1). After applying a Fourier transform with respect to time each frequency slice of this new cube represents the data matrix,  $\mathbf{P}$ .

In the data matrix,  $\mathbf{P}$ , each column corresponds to a monochromatic common-shot gather (see Figure 2-2), each row to a monochromatic common-receiver gather, each diagonal to a monochromatic common-offset gather, and each anti-diagonal to a monochromatic common-midpoint gather.

According to the seismic forward model of [Berkhout \(1982\)](#) the data matrix,  $\mathbf{P}$ , can be represented by a matrix multiplication of the source matrix,  $\mathbf{S}$ , the impulse response of the earth,  $\mathbf{X}$ , and the receiver matrix,  $\mathbf{D}$ :

$$\mathbf{P} = \mathbf{D} \mathbf{X} \mathbf{S}. \quad (2-1)$$

In the source matrix,  $\mathbf{S}$ , both rows and columns represent shot positions (see Figure 2-3). Thus,  $\mathbf{S}$  is a diagonal matrix. Each diagonal element  $s_{ii}$  captures one frequency component of the source signature injected in the earth at the position  $x_s = x_i$ . By applying a Fourier

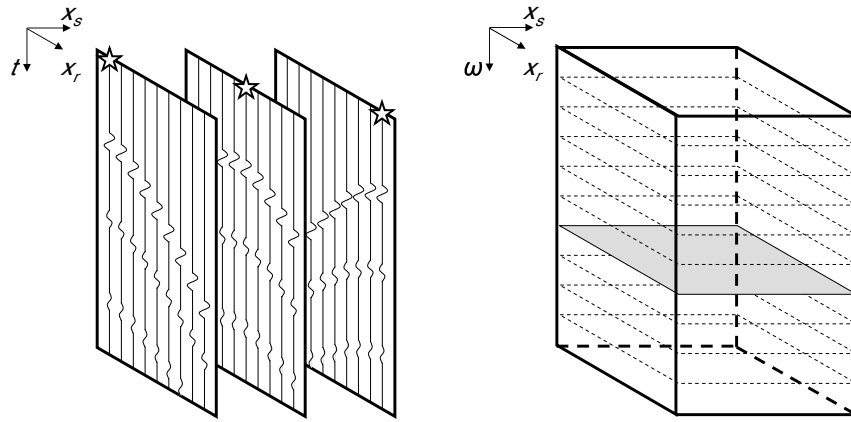


**Figure 2-1:** Illustration of the data matrix,  $\mathbf{P}$ , by [van Groenestijn \(2010\)](#). *Left:* The signal generated at the source position,  $x_s$ , is measured at receiver position,  $x_r$ , as a function of time,  $t$ . Thus, the discretized data is saved in a cube,  $\mathbf{p}(t, x_r, x_s)$ . *Right:* The cube on the right equals the left cube after a Fourier transform with respect to time. Each frequency slice of the right cube represents the data matrix,  $\mathbf{P}$ .

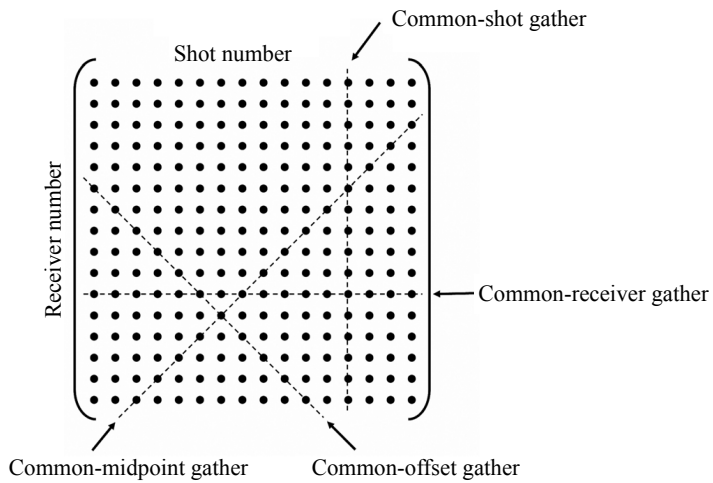


**Figure 2-2:** Illustration of the data matrix,  $\mathbf{P}$ , by [Mahdad et al. \(2011\)](#). The dotted lines indicate directions of common gathers.

$$\begin{array}{|c|c|c|c|} \hline
 \star & 0 & 0 & 0 \\ \hline
 0 & \star & 0 & 0 \\ \hline
 0 & 0 & \star & 0 \\ \hline
 0 & 0 & 0 & \star \\ \hline
 \end{array}
 \cdot
 \begin{array}{|c|c|} \hline
 1 & 0 \\ \hline
 0 & 1 \\ \hline
 e^{-j\omega\Delta t_1} & 0 \\ \hline
 0 & e^{-j\omega\Delta t_2} \\ \hline
 \end{array}
 =
 \begin{array}{|c|c|} \hline
 \star & 0 \\ \hline
 0 & \star \\ \hline
 \star & 0 \\ \hline
 0 & \star \\ \hline
 \end{array}$$

**S**                     **$\Gamma$**                      **$S_{bl}$**

**Figure 2-3:** A conventional source matrix,  $\mathbf{S}$ , is transformed to a blended source matrix,  $\mathbf{S}_{bl}$ , by applying the blending matrix,  $\mathbf{\Gamma}$ . Each star represents one shot, and the gray scale of the stars represents the relative firing-time.

transform to all frequency components of the element  $s_{ii}$  the source signature as a function of time is obtained.

The impulse response of the earth,  $\mathbf{X}$ , describes how an impulse at the source location,  $x_s$ , is transformed in the earth into the signal at the receiver location,  $x_r$ .

The receiver matrix,  $\mathbf{D}$ , converts the seismic wavefield at the receiver location,  $x_r$ , to the recorded signal. This includes adding the receiver ghost.

In practice, one tries to retrieve the unknown earth response,  $\mathbf{X}$ , from the data,  $\mathbf{P}$ , by removing  $\mathbf{S}$  (designation) and  $\mathbf{D}$  (receiver deghosting).

### 2-1-2 Blended Seismic Data

In blended acquisition the recorded events belonging to different shots overlap, as shown in the shot gather in Figure 2-4.

Blending can be captured in the forward model by introducing a blending matrix,  $\mathbf{\Gamma}$ , which transforms the source matrix,  $\mathbf{S}$ , into a blended source matrix,  $\mathbf{S}_{bl}$ ,

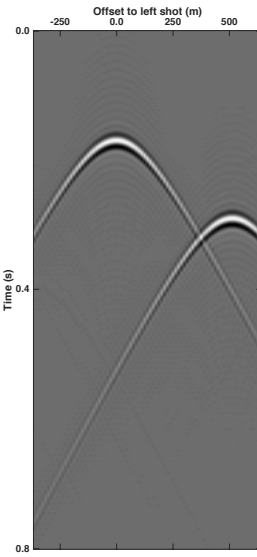
$$\mathbf{S}_{bl} = \mathbf{S} \mathbf{\Gamma}. \quad (2-2)$$

Figure 2-3 shows the structure of  $\mathbf{\Gamma}$ ; each row of  $\mathbf{\Gamma}$  represents one source, and each column of  $\mathbf{\Gamma}$  represents one experiment with multiple shots.

The blending matrix captures the physics of a blended acquisition as follows: An element  $\gamma_{ij}$  of the blending matrix includes a source  $i$  and an experiment  $j$ . If the source  $i$  is not fired in the  $j^{th}$  experiment  $\gamma_{ij}$  is zero. If it is fired, source  $i$  has a relative amplitude  $A_{ij}$  and a relative time delay  $\Delta t_{ij}$  with respect to the first source fired in the  $j^{th}$  experiment;

$$\gamma_{ij} = A_{ij} e^{-j\omega\Delta t_{ij}}. \quad (2-3)$$

Thus, the blending matrix selects specific sources from the source matrix and superimposes them as visualized in Figure 2-3. From Figure 2-3 it also becomes clear that both the blending



**Figure 2-4:** Blended shot gather of two shots. The right shot is fired 120 ms after the left shot.

matrix,  $\Gamma$ , and the blended source matrix,  $\mathbf{S}_{bl}$ , have more rows than columns, i.e. there are more sources than experiments. Thus, the acquisition is done in less time.

In the case of source blending the receiver matrix,  $\mathbf{D}$ , is not influenced. Of course, the earth impulse response,  $\mathbf{X}$ , is independent of the acquisition design. Hence, the blended data can be written as;

$$\mathbf{P}_{bl} = \mathbf{D} \mathbf{X} \mathbf{S}_{bl} = \mathbf{D} \mathbf{X} \mathbf{S} \Gamma = \mathbf{P} \Gamma. \quad (2-4)$$

Note that, the blended data matrix,  $\mathbf{P}_{bl}$ , also has less columns, i.e. less experiments, than the unblended data matrix,  $\mathbf{P}$ .

## 2-2 Deblending

Before removing the receiver matrix,  $\mathbf{D}$ , and the source matrix,  $\mathbf{S}$ , one must remove the blending matrix,  $\Gamma$ , from the blended data,  $\mathbf{P}_{bl}$ . This process is called deblending.

The deblending method presented in this thesis builds on the method of [Mahdad et al. \(2011\)](#). Therefore, this method is described in more detail.

The basic workflow of the Mahdad method is summarized in Figure 2-5 and will be explained step by step in the following subsections.

### 2-2-1 Pseudo-Deblending

Unfortunately, the inverse problem of equation 2-4 is underdetermined, which means that there is not a unique solution for the unblended data,  $\mathbf{P}$ . Thus, additional constraints are

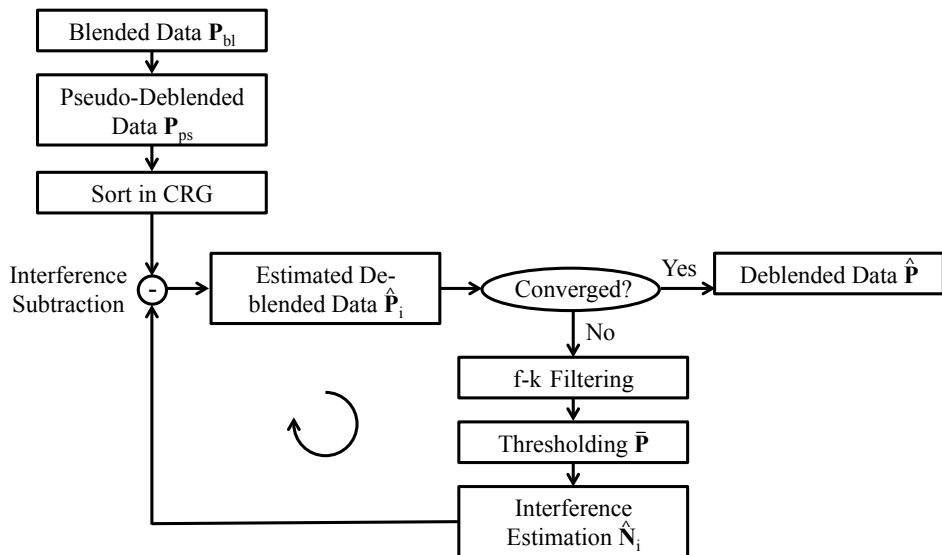


**Figure 2-5:** Flowchart belonging to the deblending method of Mahdad et al. (2011).

required to deblend the data, which are; (1) sparsity of the signal in the  $x$ - $t$ -domain and (2) coherency of the signal in the  $f$ - $k$  domain.

The first estimate of the unblended data matrix,  $\mathbf{P}$ , is obtained by pseudo-deblending;

$$\mathbf{P}_{ps} = \mathbf{P}_{bl} \boldsymbol{\Gamma}^H, \quad (2-5)$$

where  $\boldsymbol{\Gamma}^H$  is the conjugate transpose of the blending matrix,  $\boldsymbol{\Gamma}$ . Pseudo-deblending copies the blended data to the locations of all shots present in the blended shot and shifts them upward in time to compensate for the time delay. For example, Figure 2-6a and 2-6b shows the two pseudo-deblended shot gathers of the blended data in Figure 2-4. Note that the pseudo-deblended data,  $\mathbf{P}_{ps}$ , have the same size as  $\mathbf{P}$ .

## 2-2-2 Common-Receiver Gather

In Figure 2-6a and 2-6b the interfering shot is coherent. By transforming the data to another domain, e.g. to the common-receiver domain, the interfering shot becomes incoherent and is visible as spiky noise (see Figure 2-6c). Therefore, the interfering shots can be attenuated with a noise filter in the common-receiver domain.

definition  
of inco-  
herency?

## 2-2-3 Iterative Estimation of Blending Noise

In an ideal case the noise generated by the interfering shots present in the pseudo-deblended data, the so-called blending noise, is calculated with the unblended data,

$$\mathbf{N} = \mathbf{P}_{bl} \boldsymbol{\Gamma}^H - \mathbf{P} = \mathbf{P}_{ps} - \mathbf{P}. \quad (2-6)$$

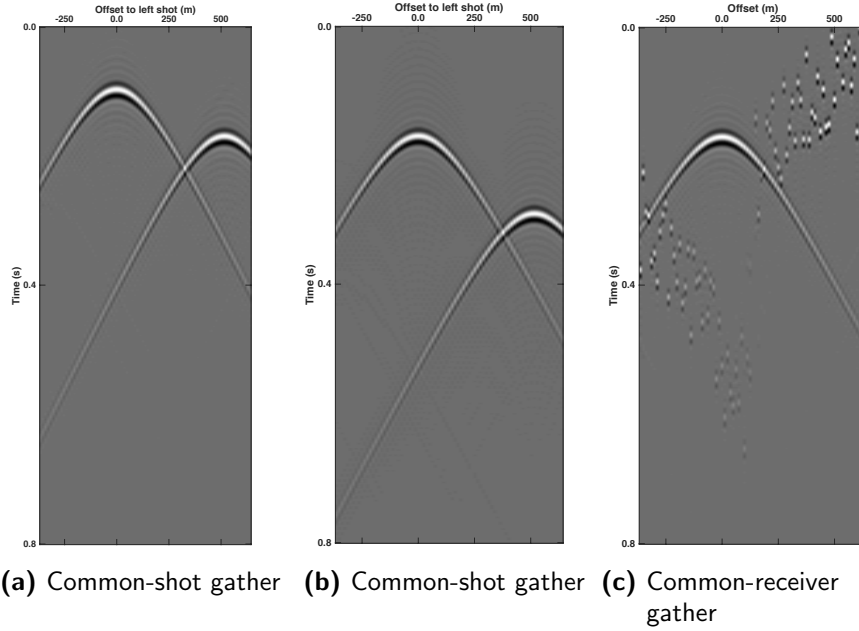


**Figure 2-6:** Pseudo-deblended data,  $\mathbf{P}_{ps}$ , sorted in common-shot gathers (a,b) and in a common-receiver gather (c). The pseudo-deblended data of the right shot (a) and the left shot (b,c) were shifted by different time delays. The overlapping sources map in the pseudo-deblended shot gathers as coherent events, while they map as incoherent spikes in the pseudo-deblended receiver gather.

Obviously, in practice the unblended data are unknown and are estimated by adding extra constraints. The loop shown in Figure 2-5 uses the pseudo-deblended data,  $\mathbf{P}_{ps}$ , as an initial estimation of the unblended data. Next, it applies the constraints to reduce the blending noise iteratively until the solution is obtained.

In the following all the quantities which are estimated are indicated with a hat. The steps of the iterative blending noise estimation are illustrated in Figure 2-7.

### f-k Filtering

One of the constraints is coherency, i.e. by assuming the blending noise in Figure 2-7a is incoherent it can be removed. For this purpose the data are transformed from the space-time to the wavenumber-frequency domain where the spiky noise spreads over all wavenumber and frequency components (see Figure 2-7b, top).

The unblended data would map in the *f-k* domain in a cone (see Figure 2-8a). The minimum wavefield velocity present in the subsurface,  $v_{min}$ , determines the slope of the cone. This means that for a given frequency,  $f$ , the maximum wavenumber inside the cone,  $k_{max}$ , is defined as;

$$k_{max} = \frac{f}{v_{min}}. \quad (2-7)$$

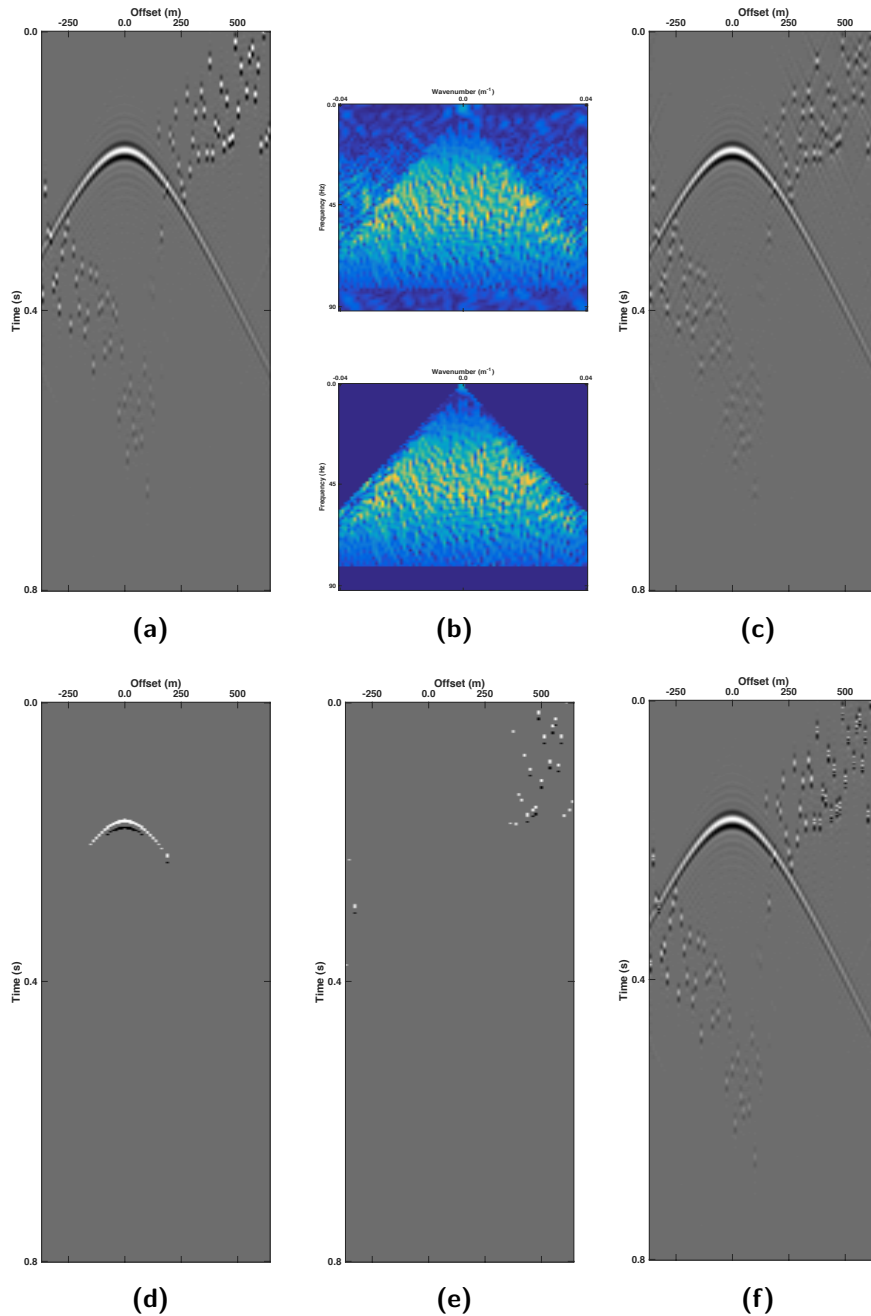
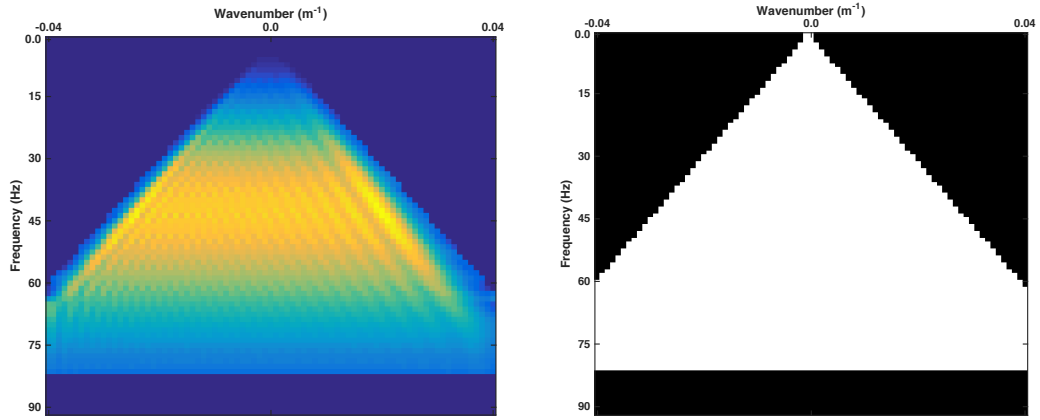


**Figure 2-7:** (a) Pseudo-deblended receiver gather. The subfigures (b)-(f) illustrate each step of the deblending algorithm. For better visibility examples from the 5<sup>th</sup> iteration are chosen. (b)  $f\text{-}k$  spectrum before (top) and after (bottom)  $f\text{-}k$  filtering, (c)  $f\text{-}k$  filtered common-receiver gather, (d) after thresholding, (e) estimated blending noise, (f) estimated data.



(a)  $f\text{-}k$ -spectrum of an unblended common-shot gather.

(b) The  $f\text{-}k$ -mask is determined by the minimum signal velocity in the subsurface. The white area of the filter equals one, the black area equals zero. Thus, the filter removes data which are mapped outside of the white signal cone.

**Figure 2-8**

In the marine case the minimum velocity is usually the water velocity,  $v_w = 1500 \text{ m s}^{-1}$ .

A 2D  $f\text{-}k$  filter can be designed that removes all elements outside the cone (see Figure 2-8b). The  $f\text{-}k$  filter removes the part of the blending noise, which maps outside of the signal cone (see Figure 2-7b). Thus, after transforming the data back to the space-time domain the amplitudes of the spiky noise are attenuated (see Figure 2-7c).

Note that  $f\text{-}k$  filtering can only reduce spatially unaliased blending noise. In Figure 2-8b the highest spatially unaliased frequency is defined by the point where the white cone intersects with the frequency axis, i.e. at 60 Hz. The spatially aliased blending noise will pass the  $f\text{-}k$  filter and will be reduced afterwards by thresholding.

The high cut frequency of the  $f\text{-}k$  mask,  $f_{cut} = 80 \text{ Hz}$ , is set according to the highest frequency components in the data.

### Thresholding

The second constraint for the estimation of the unblended data is sparsity of the signal in the space-time domain.

After  $f\text{-}k$  filtering the spiky noise is attenuated (see Figure 2-7c). Consequently, the signal amplitudes are now stronger than the noise amplitudes. This allows to define a threshold in the  $x\text{-}t$  domain, which is larger than the attenuated noise amplitudes and smaller than the highest signal amplitudes. Only amplitudes above the threshold are picked (see Figure 2-7d).

### Interference Estimation

The resulting thresholded data,  $\bar{\mathbf{P}}$ , is used to predict the blending noise;

$$\hat{\mathbf{N}}_i = \bar{\mathbf{P}} (\mathbf{\Gamma} \mathbf{\Gamma}^H - \mathbf{I}), \quad (2-8)$$

which is illustrated in Figure 2-7e.

### Blending Noise Subtraction

The estimate of the unblended data matrix  $\hat{\mathbf{P}}_i$  is updated by subtracting the estimated blending noise from the pseudo-deblended data,

$$\hat{\mathbf{P}}_{i+1} = \mathbf{P}_{ps} - \hat{\mathbf{N}}_i, \quad (2-9)$$

which is shown in Figure 2-7f.

This process is repeated iteratively till convergence is reached. In this context convergence can be defined as the point where the difference  $| \hat{\mathbf{P}}_{i+1} - \hat{\mathbf{P}}_i |$  drops below a predefined limit. Alternatively, one can set a maximum number of iterations.

Figure 2-9 shows the estimate of the unblended data for increasing iterations. At each iteration the blending noise is attenuated further, such that the threshold can be lowered. Hence, the predicted blending noise increases and approaches the true blending noise. The two blended shots are successively deblended.

Note that,  $f\text{-}k$  filtering lowers the noise level by removing spatially unaliased blending noise. Next, the lowered noise level enables thresholding to reduce spatially aliased blending noise. Thus, the combination of  $f\text{-}k$  filtering and thresholding is very powerful.

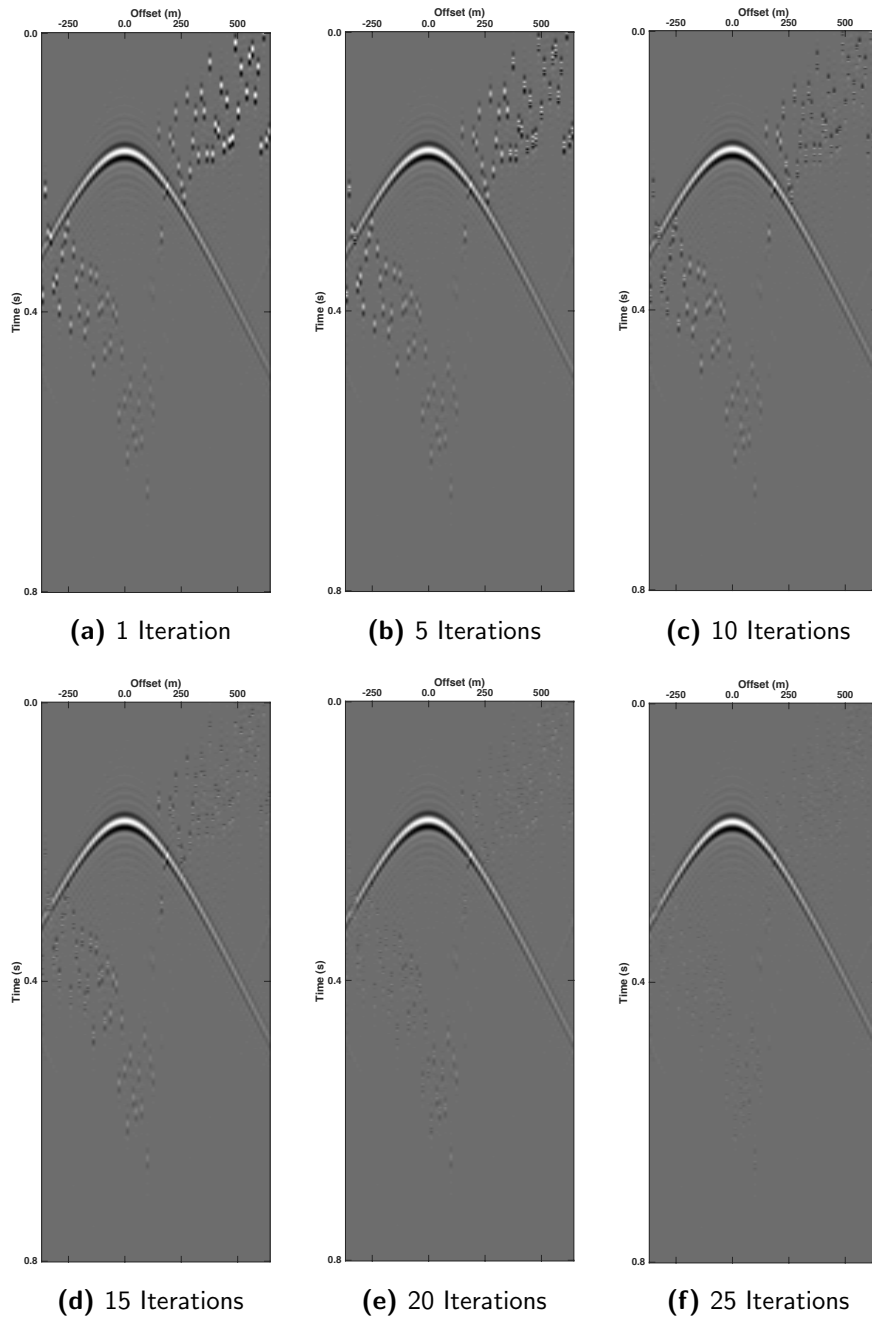


**Figure 2-9:** Common-receiver gather of the estimated data after 1, 5, 10, 15, 20 and 25 iterations.

---

# Chapter 3

---

## Incoherency

In this chapter the blending operator is analyzed in greater detail. The analysis aims to propose a blending operator which facilitates deblending. Before starting the analysis a new measure of incoherency is introduced. Then, it is discussed how incoherency and the so-called maximum firing-time delay influence deblending.

### 3-1 Analysis of the Blending Matrix

In order to optimize the blended acquisition design, one must understand the properties of the blending matrix,  $\Gamma$ , and its influence on the deblending performance.

The blending matrix,  $\Gamma$ , determines the pseudo-deblended data,

$$\mathbf{P}_{ps} = \mathbf{P}\Gamma\Gamma^H, \quad (3-1)$$

which are a superposition of the unblended data,  $\mathbf{P}$ , and the blending noise,  $\mathbf{N}$ ,

$$\mathbf{P}_{ps} = \mathbf{P} + \mathbf{N} = \mathbf{P}\mathbf{I} + \mathbf{P}(\Gamma\Gamma^H - \mathbf{I}). \quad (3-2)$$

The more incoherent the blending noise,  $\mathbf{N}$ , the better it can be removed by noise filters.

In the following the effect of the blending matrix,  $\Gamma$ , on the pseudo-deblended data,  $\mathbf{P}_{ps}$ , is analyzed. For simplicity, it is assumed that all shots are equal in strength and fire the same signature into the earth. It is also assumed that each shot is fired only once, unlike e.g. the shot repetition case (Wu, 2014). This means that the blending matrix,  $\Gamma$ , only contains phase shift terms,  $e^{-j\omega\Delta t}$ , or zeros.

Each row of  $\Gamma$  represents a shot  $k$ , and each column of  $\Gamma^H$  represents a shot  $l$  with a complex conjugated phase term (see Figure 3-1). Hence, each element  $g_{kl}$  of the matrix  $\Gamma\Gamma^H$  is the dot product between the  $k^{th}$  shot and the complex conjugate of the  $l^{th}$  shot.

$$\begin{array}{c}
 \text{shot } k \\
 \left[ \begin{array}{|c|c|} \hline e^{-j\omega\Delta t_i} & 0 \\ \hline 0 & e^{-j\omega\Delta t_k} \\ \hline e^{-j\omega\Delta t_j} & 0 \\ \hline 0 & e^{-j\omega\Delta t_l} \\ \hline \end{array} \right] \cdot \left[ \begin{array}{|c|c|c|c|} \hline & \text{shots} & & * \\ \hline e^{+j\omega\Delta t_i} & 0 & e^{+j\omega\Delta t_j} & 0 \\ \hline 0 & e^{+j\omega\Delta t_k} & 0 & e^{+j\omega\Delta t_l} \\ \hline \end{array} \right] = \left[ \begin{array}{|c|c|c|c|} \hline 1 & 0 & e^{-j\omega\Delta t_{ij}} & 0 \\ \hline 0 & 1 & 0 & e^{-j\omega\Delta t_{kl}} \\ \hline e^{-j\omega\Delta t_{ji}} & 0 & 1 & 0 \\ \hline 0 & e^{-j\omega\Delta t_{lk}} & 0 & 1 \\ \hline \end{array} \right] \\
 \Gamma \qquad \qquad \qquad \Gamma^H \qquad \qquad \qquad \Gamma\Gamma^H
 \end{array}$$

**Figure 3-1:** Illustration of the matrix product,  $\Gamma\Gamma^H$ . In this notation  $\Delta t_k$  refers to the phase shift of the shot  $k$ , and  $\Delta t_{kl}$  refers to the phase shift between the shots  $k$  and  $l$ ,  $\Delta t_{kl} = \Delta t_k - \Delta t_l$ .

Consequently, an element  $g_{kl}$  of the matrix product,  $\Gamma\Gamma^H$ , represents the overlap of the shots  $k$  and  $l$  for all experiments. The main diagonal of  $\Gamma\Gamma^H$  refers to the overlap of each shot with itself, which of course is perfect and therefore equal to 1. The off-diagonal elements of  $\Gamma\Gamma^H$  are either 0 if the associated shots do not overlap, or contain a phase shift,  $e^{-j\omega\Delta t_{kl}}$ .

### Temporal incoherency

In the following the term "sub-diagonal" will be used to refer to an arbitrary diagonal of the matrix  $\Gamma\Gamma^H$ . For example, the  $d^{th}$  sub-diagonal includes all the matrix elements  $g_{ij}$ , which fulfill the condition;  $j - i = d$ .

In equation 3-2 the main diagonal elements of  $\Gamma\Gamma^H$  copy the data matrix,  $\mathbf{P}$ , while the off-diagonal elements create the blending noise,  $\mathbf{N}$ . In case of constant firing-time delays the elements along a sub-diagonal  $d$  all have the same phase. This means that the sub-diagonal elements will shift the columns of the data matrix and apply a constant phase shift to each of them resulting in the pseudo-deblended receiver gather shown in Figure 3-2a. Instead if firing-times are not constant but random the elements  $g_{ij}$  along a sub-diagonal  $d$  will have different phases. Consequently, they will shift the columns of the data matrix and distort the phase of each column (see Figure 3-2b).

Figure 3-2c and 3-2d display the  $f$ - $k$  spectra of the pseudo-blended data for constant firing-time delays and random firing-time delays respectively. In the case of constant firing-time delays all of the energy maps in the signal cone. In the case of random firing-time delays a significant part of the energy maps outside of the signal cone. From Figure 3-2c and 3-2d it is clear that the coherency constraint presented in section 2-2-3 cannot work with constant firing-time delays, but needs the random firing-time delays.

In this thesis the random firing-time delays along a sub-diagonal are referred to as temporal incoherency.

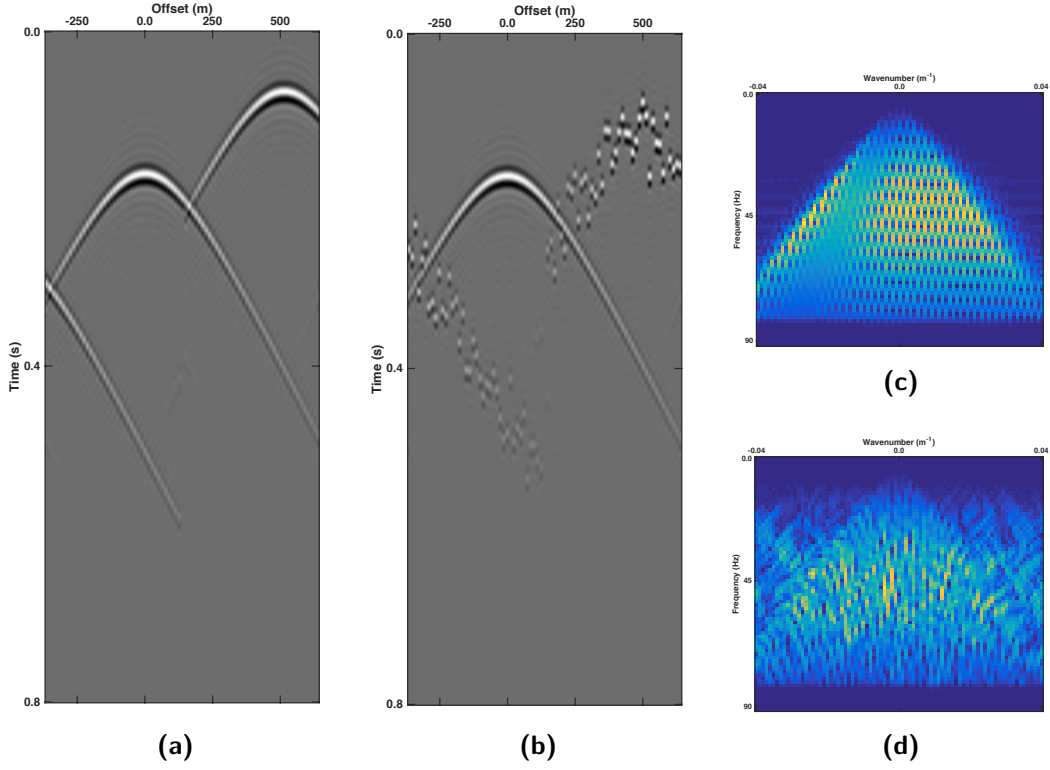


**Figure 3-2:** Comparison of the pseudo-deblended receiver gather for (a) constant firing-time delays of 100 ms, and (b) random firing-time delays between 0 ms and 100 ms. (c) and (d) show the  $f$ - $k$  spectra of (a) and (b) respectively.

$$\begin{array}{c}
 \begin{array}{|c|c|} \hline
 e^{-j\omega\Delta t_i} & 0 \\ \hline
 0 & e^{-j\omega\Delta t_k} \\ \hline
 0 & e^{-j\omega\Delta t_l} \\ \hline
 e^{-j\omega\Delta t_j} & 0 \\ \hline
 \end{array} \cdot \begin{array}{|c|c|c|c|} \hline
 & & \text{shot } k & * \\ \hline
 e^{+j\omega\Delta t_i} & 0 & 0 & e^{+j\omega\Delta t_j} \\ \hline
 0 & e^{+j\omega\Delta t_k} & e^{+j\omega\Delta t_l} & 0 \\ \hline
 \end{array} = \begin{array}{|c|c|c|c|} \hline
 1 & 0 & 0 & e^{-j\omega\Delta t_{ij}} \\ \hline
 0 & 1 & e^{-j\omega\Delta t_{kl}} & 0 \\ \hline
 0 & e^{-j\omega\Delta t_{lk}} & 1 & 0 \\ \hline
 e^{-j\omega\Delta t_{ji}} & 0 & 0 & 1 \\ \hline
 \end{array} \\
 \Gamma \qquad \qquad \qquad \Gamma^H \qquad \qquad \qquad \Gamma \Gamma^H
 \end{array}$$

**Figure 3-3:** The blending matrix,  $\Gamma$ , is obtained by interchanging the 3<sup>rd</sup> and 4<sup>th</sup> row of the blending matrix in Figure 3-1. In acquisition this is equivalent to moving shot 3 to experiment 2, and shot 4 to experiment 1. A random permutation of the rows of the blending matrix spreads the off-diagonal elements of the matrix product,  $\Gamma \Gamma^H$ . The elements are not assembled on the sub-diagonals anymore.

## Spatial incoherency

Of course, the degree of incoherency of the blending noise,  $\mathbf{N}$ , also depends on whether the shot positions of shots blended in an experiment are selected randomly, or in a spatially coherent pattern. For example, one expects the blending noise to be more incoherent if in each experiment randomly selected shot positions are blended as in Figure 3-3, than if in each experiment adjacent shot positions are blended as in Figure 3-1, because the interfering shots are spread over the sub-diagonals in Figure 3-3.

In this thesis selecting random shots for an experiment is referred to as spatial incoherency.

Although examples of spatial incoherency are shown in this chapter, it has to be noted that to blend shots in a spatially incoherent fashion is not very practical in 2D acquisition. However, in chapter 4 it will be shown that for 3D blending spatial incoherency becomes feasible.

## 3-2 Results Spatial and Temporal Incoherency

Based on the blending matrices in Figure 3-1 and 3-3 there are three possibilities to blend the shots incoherently. First, the phase terms along the sub-diagonals can be randomly varied, i.e. the shots are blended with random firing-time delays (temporal incoherency). Second, the rows of the blending matrix can be randomly permuted, i.e. one randomly selects shots for each experiment (spatial incoherency). Third, temporal and spatial incoherency can be combined (mixed incoherency), i.e. randomly selected shots are blended with random firing-time delays.

These 3 blending patterns are applied to a synthetic data set. The data are a common-receiver gather with 21 shots (see Figure 3-4a), which are blended in 3 experiments with 7 shots per experiment. Next, the data are deblended with the deblending algorithm of section 2-2.

The deblended receiver gathers are shown in Figure 3-4. The results suggest that only spatial incoherency is not sufficient to deblend the data (see Figure 3-4b). By introducing random firing-time delays the deblended data improve significantly as shown in Figure 3-4c. A combination of both spatial and temporal incoherency enhances the deblended data further (see Figure 3-4d).

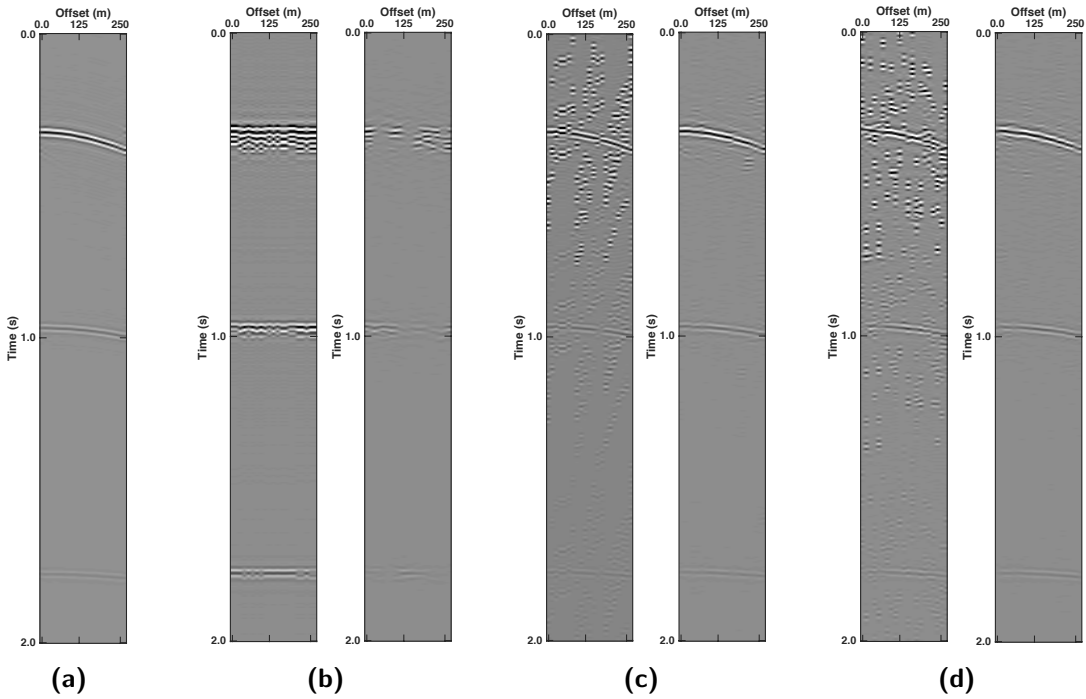


**Figure 3-4:** (a) shows a synthetic unblended common-receiver gather. The data are blended with a (b) spatially incoherent, (c) temporally incoherent, and (d) mixed incoherent blending pattern. The respective pseudo-deblended data (left) and deblended data (right) are shown in (b) to (d).

### 3-3 Effect of Incoherency

This section aims to analyze how strongly the deblending result depends on the incoherency of the blended acquisition. For this purpose a measure of incoherency and deblending quality will be introduced.

#### Incoherency Measure

Move this sentence to the introduction (literature). You might also want to mention the work of the Greek guy Apostolos.

In this thesis only the incoherency of the acquisition design is considered. Thus, the blending matrix,  $\Gamma$ , or more precisely the product  $\Gamma\Gamma^H$  determines the incoherency.

In section 3-1 it was shown that for an incoherent blending pattern the elements,  $e^{-j\omega\Delta t_{kl}}$ , along a sub-diagonal of the matrix product,  $\Gamma\Gamma^H$ , should be out of phase, i.e. each element should contain a different time delay,  $\Delta t$ . Therefore, the phase variability of the sub-diagonal elements will be used to quantify incoherency.

The sub-diagonal elements,  $e^{-j\omega\Delta t_{kl}}$ , map in the complex plane on a circle with radius 1 (see Figure 3-5). Thus, the sum of the elements along the  $d^{th}$  sub-diagonal can be constructive or destructive, depending on the phase variability. The absolute value of this sum,  $M(d, \omega)$ , measures the incoherency of the  $d^{th}$  sub-diagonal for the frequency component,  $\omega$ ;

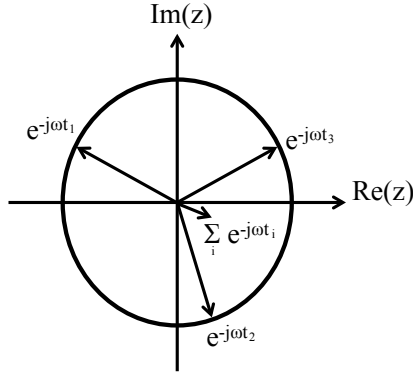


**Figure 3-5:** Illustration of the sub-diagonal elements in the complex number plane. The elements have unit length and variable phase. The absolute value of their sum depends on the phase coherency of the elements.

$$M(d, \omega) = \left| \sum_{j-i=d} \boldsymbol{\Gamma} \boldsymbol{\Gamma}_{ij}^H(\omega) \right|. \quad (3-3)$$

If all sub-diagonal elements are in phase the absolute value of their sum,  $M(d, \omega)$ , is maximized. Instead, in case of an incoherent blending pattern  $M(d, \omega)$  is small for all sub-diagonals  $d$ , except for the main diagonal ( $d = 0$ ).

The incoherency measure,  $\mu$ , is introduced as;

$$\mu = \frac{(\sum_{\omega} M(d=0, \omega))^2}{\sum_{d=1-N_s}^{N_s-1} ((\sum_{\omega} M(d, \omega))^2)}, \quad (3-4)$$

where  $N_s$  is the number of sources, i.e. the matrix  $\boldsymbol{\Gamma} \boldsymbol{\Gamma}^H$  has  $N_s$  rows and columns. Note that in this ratio, the numerator relates to the main diagonal only, and the denominator to all sub-diagonals.

Equation 3-4 implies that the incoherency value can vary between 0 (perfectly coherent) and 1 (perfectly incoherent).

For example, consider the two blending matrices,  $\boldsymbol{\Gamma}_{coh}$  and  $\boldsymbol{\Gamma}_{ran}$ , which produce the pseudo-deblended receiver gathers in Figure 3-2a and 3-2b respectively. The blending matrix,  $\boldsymbol{\Gamma}_{coh}$ , uses constant firing-time delays, while the blending matrix,  $\boldsymbol{\Gamma}_{ran}$ , uses random firing-time delays. Figure 3-6 shows  $M(d, \omega)$  for both blending matrices for the frequency slice  $f = 25$  Hz. One can observe that for the incoherent blending matrix,  $\boldsymbol{\Gamma}_{ran}$ ,  $M(d, \omega)$  resembles a simple spike more than for the coherent blending matrix,  $\boldsymbol{\Gamma}_{coh}$ . The coherent blending matrix,  $\boldsymbol{\Gamma}_{coh}$ , yields an incoherency value of  $\mu_{coh} = 67\%$ , whereas the incoherent blending matrix,  $\boldsymbol{\Gamma}_{ran}$ , yields an incoherency value of  $\mu_{ran} = 98\%$ .

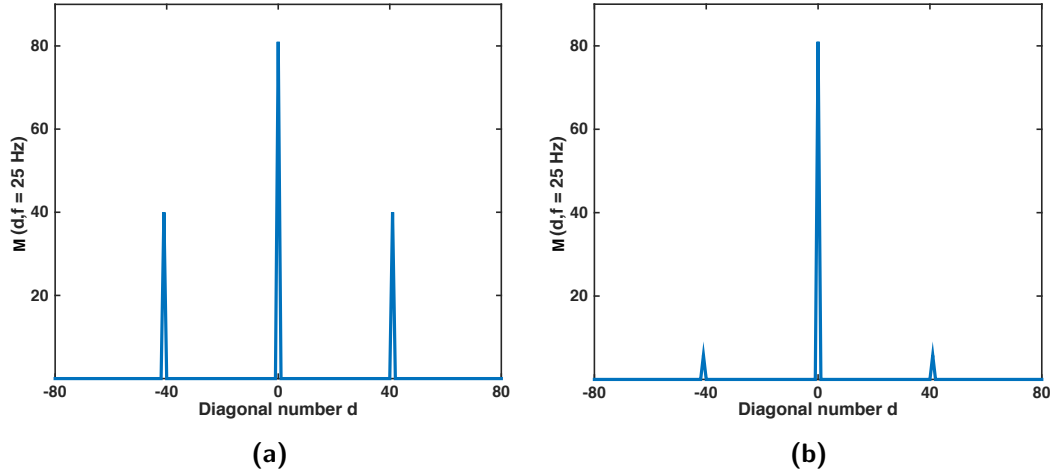


**Figure 3-6:** Illustration of the absolute sub-diagonal sums,  $M(d, \omega)$ , for the frequency slice  $f = 25 \text{ Hz}$ . (a) refers to the blending matrix  $\Gamma_{coh}$  with constant firing-time delays. (b) refers to the blending matrix  $\Gamma_{ran}$  with random firing-time delays.

### Deblending Performance Measure

The following data examples are synthetic data, i.e. the unblended data are known. Therefore, the deblending performance can be measured with the quality factor,  $Q$ , which is defined by Ibrahim and Sacchi (2015) as;

$$Q = 10 \cdot \log_{10} \left( \frac{\|\mathbf{P}\|_2^2}{\|\mathbf{P} - \hat{\mathbf{P}}\|_2^2} \right), \quad (3-5)$$

where  $\mathbf{P}$  are the unblended data, and  $\hat{\mathbf{P}}$  the deblended data. This is similar to the definition of signal to noise ratio.

### 3-4 Results Incoherency

Consider again the two blending matrices,  $\Gamma_{coh}$  and  $\Gamma_{ran}$ , which produced the pseudo-deblended receiver gathers in Figure 3-2a and 3-2b respectively. Both blending matrices use the same maximum firing-time delay, while their incoherency values differ ( $\mu_{coh} = 67\%$ ,  $\mu_{ran} = 98\%$ ).

An effective blending matrix,  $\Gamma_{eff}$ , is created by superimposing the time delays  $e^{-j\omega\Delta t_{ij}}$  of the blending matrices  $\Gamma_{coh}$  and  $\Gamma_{ran}$ ;

$$\Delta t_{eff} = a \cdot \Delta t_{ij, ran} + (1 - a) \cdot \Delta t_{ij, coh}, \quad a \in [0, 1]. \quad (3-6)$$

The maximum firing-time delay of the effective blending matrix,  $\Gamma_{eff}$ , is constant while the incoherency varies with changing  $a$ . The resulting quality factors are shown as a function of the incoherency in Figure 3-7.

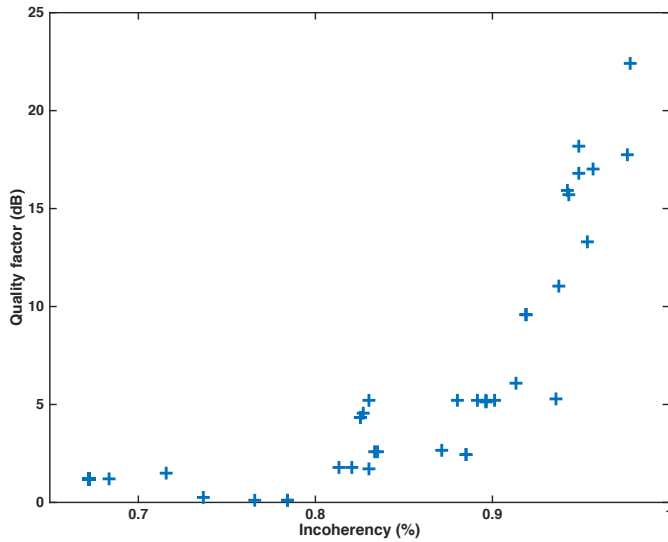


**Figure 3-7:** Deblending quality as a function of incoherency for a constant maximum firing-time delay.

One can observe that the deblending quality increases with increasing incoherency.

### 3-5 Effect of Maximum Firing-Time Delay

Another control factor of the deblending quality is the maximum firing-time delay. In an extreme case of infinitely long maximum firing-time delay the acquisition is not blended any more, and the deblending result is perfect. Hence, increasing maximum firing-time delays are expected to enhance the deblending quality. Of course, they require more acquisition time.

### 3-6 Results Maximum Firing-Time Delay

The three suggested blending patterns namely temporal, spatial and mixed incoherency are applied to synthetic data with varying maximum firing-time delays.

Figure 3-8 shows the quality factors for the three blending patterns as a function of maximum firing-time delay. Note that for a fixed maximum firing-time delay and a specific blending pattern the firing-time delays are generated with a random number generator. Consequently, the resulting quality factor varies depending on the variation of the random number series. For this reason several blending matrices are generated for each maximum firing-time delay and each blending pattern. The resulting quality factors are averaged.

According to Figure 3-8 the spatially incoherent blending pattern yields a constant deblending quality independent of the maximum firing-time delay. This is expected because it blends the sources without time delay. The deblending quality provided by the other two blending patterns continuously enhances with increasing maximum firing-time delay. The difference in deblending quality between temporal and mixed blending patterns seems to be independent of the maximum firing-time delay.

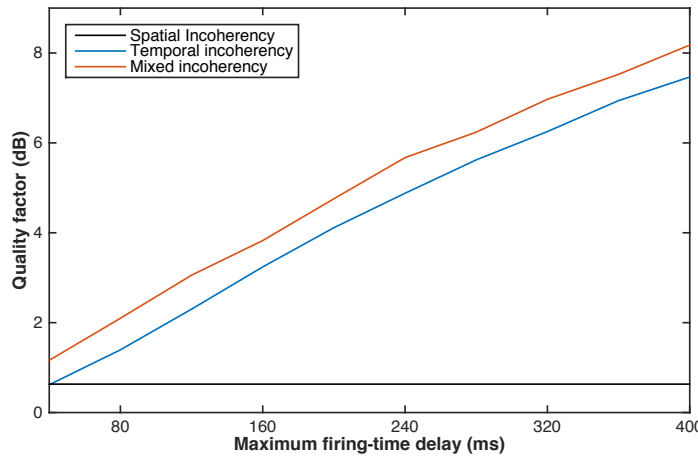


**Figure 3-8:** The 3 suggested blending patterns are simulated with maximum firing-time delays between 40 ms and 400 ms. The quality factors are computed with respect to the unblended data and illustrated as a function of the maximum firing-time delay.

## 3-7 Conclusions

It was demonstrated that successful deblending depends on; (1) the degree of incoherency, and (2) the maximum firing-time delay. These parameters are linked to each other because a longer maximum firing-time delay gives more freedom to generate (temporal) incoherency. However, the two parameters affect the deblending quality very differently. The degree of incoherency influences the deblending quality step-like (see Figure 3-7), i.e. either the incoherency is sufficiently high to deblend the data, or it is not and the deblending result is poor. The maximum firing-time delay shows an almost linear effect on the deblending quality (see Figure 3-8). Thus, the maximum firing-time delay allows to adjust the desired deblending quality.

In practice, the maximum firing-time delay will be limited by the schedule of the seismic survey. Hence, for a given maximum firing-time delay the blending pattern must be designed sufficiently incoherent to achieve the desired deblending quality. Of course, if the maximum firing-time delay is too short, it is not possible to achieve a sufficiently high degree of incoherency to deblend the data. In such a case the maximum firing-time delay must be increased.



---

## Chapter 4

---

# Crossline Deblending (3D)

This thesis proposes to blend crossline sources. It is hypothesized that by combining several cross-lines one can effectively blend sources in 3D.

The deblending method of [Mahdad et al. \(2011\)](#) described in section 2-2 is designed for 2D blended data. In this chapter I will explain how each step of the Mahdad method can be extended to 3D data, and I will demonstrate its strengths and performance.

First, the data sorting will be modified such that the blended 3D data can be described using the same forward model as in section 2-1. The presented data sorting will allow to maintain all other steps of the deblending algorithm of [Mahdad et al. \(2011\)](#). Second, the 2D  $f$ - $k$  filter will be extended to a 3D  $f$ - $k_x$ - $k_y$  filter to remove noise in both crossline and inline direction.

### 4-1 Data Sorting

#### Data Matrix

In 3D acquisition the sources and receivers are distributed on a 2D surface. Thus, their locations are defined by their inline and crossline positions,  $(x, y)$ . Each data point which is measured by a source receiver pair at a specific time is therefore described by 5 coordinates, time  $t$ , receiver inline and crossline position  $(x_r, y_r)$ , and source inline and crossline position  $(x_s, y_s)$ .

Similar as in section 2-1 the 5D data "cube" will be again reorganized in a 2D data matrix according to [van Dedem \(2002\)](#) (see Figure 4-1). For this data sorting a 1D Fourier transform with respect to time is performed and a 4D frequency "slice" is selected.

The 4D "slice" is sorted in a 2D data matrix,  $\mathbf{P}$ , with as many rows as receivers and as many columns as shots. The total number of shots is obtained by multiplying the number of shots fired in each crossline and the number of shots fired in each inline. The total number of receivers is obtained likewise. Assume there are  $Ns_x$  shots per crossline. The shots of the first crossline are assigned to the first  $Ns_x$  columns of the data matrix, the shots of the

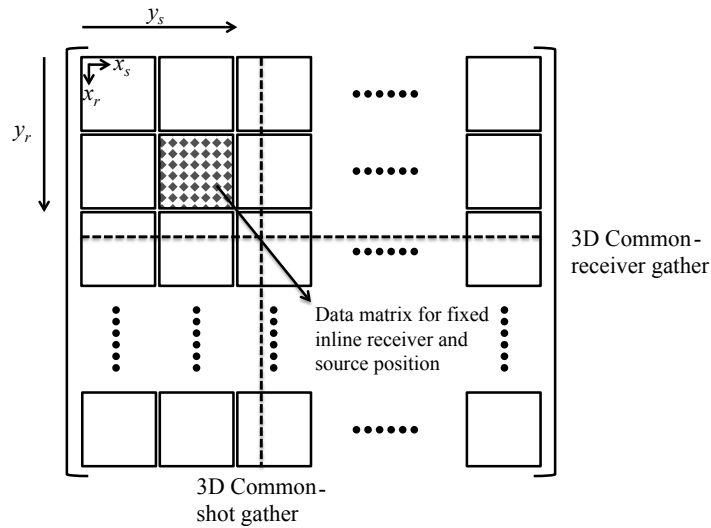


**Figure 4-1:** Illustration of the data matrix  $\mathbf{P}$  for 3D data (van Dedem, 2002).  $y_r$  and  $y_s$  represent the inline receiver and shot positions.  $x_r$  and  $x_s$  represent the crossline receiver and shot positions. Each row refers to a 3D common-receiver gather and each column to a 3D common-shot gather. A sub-matrix with fixed receiver and source inline positions ( $y_r, y_s$ ) is equivalent to a data matrix for 2D acquisition.

second crossline are assigned to the next  $Ns_x$  columns of the data matrix, etc. The receivers are sorted in the rows of the data matrix analogously.

One row in the data matrix,  $\mathbf{P}$ , in Figure 4-1 represents a 3D common-receiver gather. The data of this 3D common-receiver gather are shown in Figure 4-2a in a 3D view, where the coordinates,  $x$  and  $y$ , indicate the inline and crossline shot position respectively. For the described data sorting individual crossline slices are extracted from this data cube and assembled next to each other in a data matrix as shown in Figure 4-2b. This view will be referred to as 3D CRG 2D view. Each hyperbolic event refers to the response of the shots of one crossline.

### Blending matrix

The blending matrix for 3D is built in a similar fashion as the data matrix in 3D. As described in section 3-1 each row of the blending matrix,  $\mathbf{\Gamma}$ , captures one shot. For extension to 3D the shots of the first crossline are placed in the top  $Ns_x$  rows of the blending matrix, followed by the shots of the second crossline etc. (see Figure 4-3). The elements in the  $j^{th}$  column of the blending matrix,  $\mathbf{\Gamma}$ , select the shots which are blended in the  $j^{th}$  experiment. For example, the first column of the blending matrix in Figure 4-3b describes that in the first experiment shots (rows) 1 and 3 are blended with a time delay of  $\Delta t_1$ .

Keep this sentence for later: This framework allows to blend any source combination independent of the cross- and inline positions of the involved sources.

With the new data and blending matrix sorting one can apply deblending to 3D data in the same way as presented in section 2-1 and section 2-2. Note that unlike for 2D blending spatially incoherent blending patterns are practical for 3D blended acquisition.

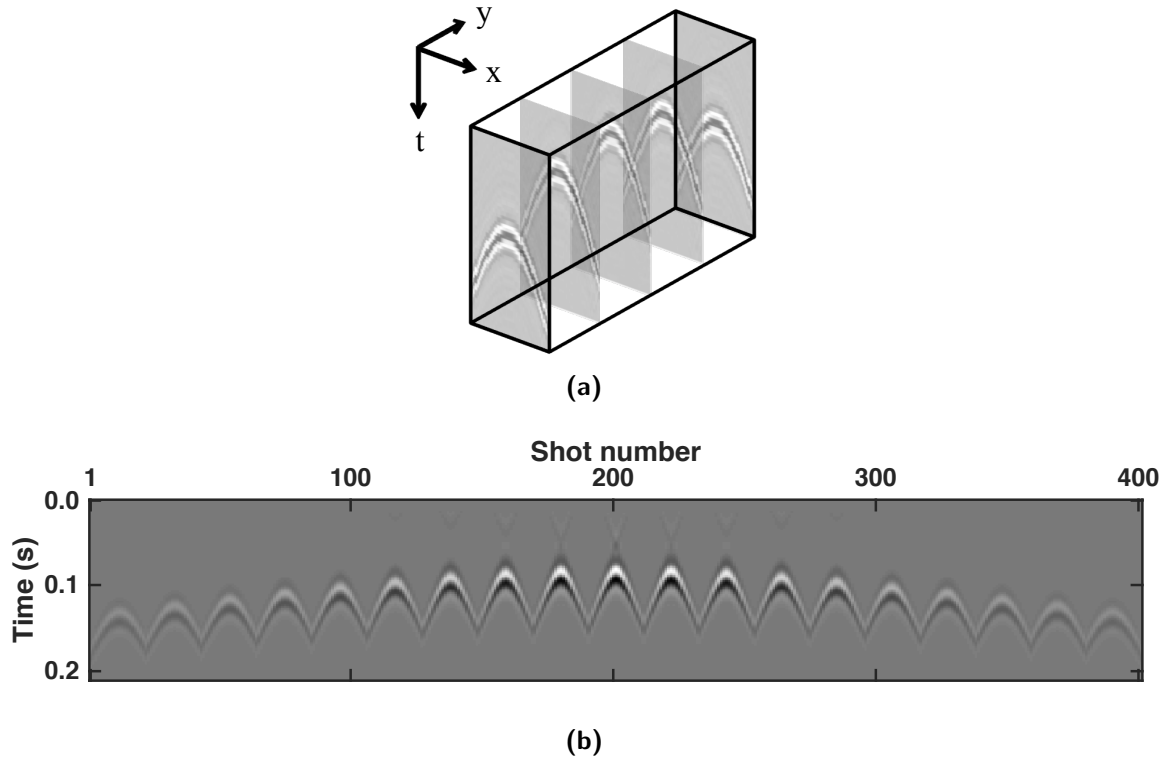


**Figure 4-2:** (a) 3D common-receiver gather with crossline ( $x$ ) and inline ( $y$ ) sources (3D view).  
 (b) Resorted data set. Individual crossline sections are plotted next to each other in 2D. For visibility both subfigures only show a reduced part of the data. This view is called 3D CRG 2D view.

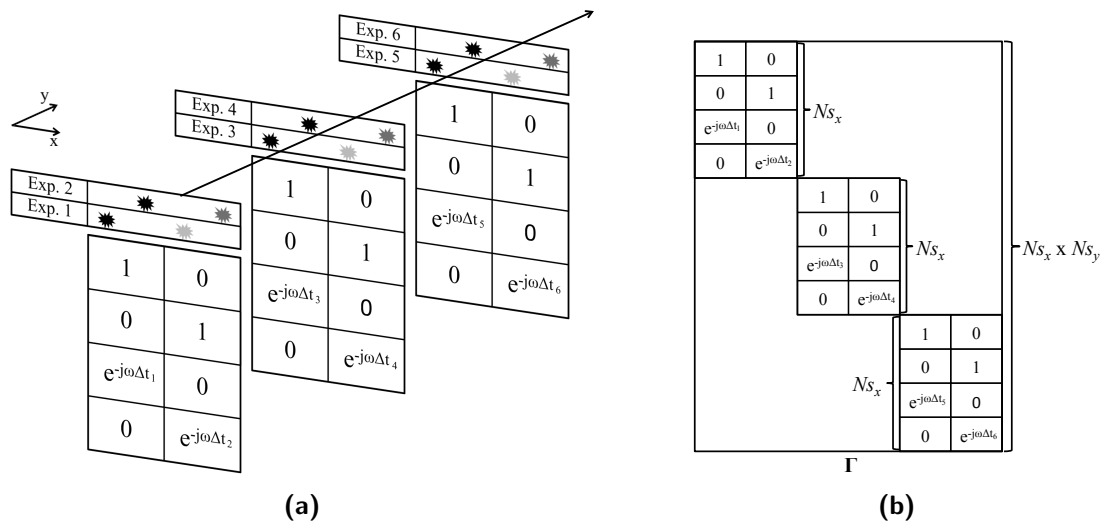


**Figure 4-3:** Illustration of the blending matrix,  $\Gamma$ , for 3D acquisition. (a) At each of the  $N_{s_y}$  inline position the crossline sources ( $x$  direction) are blended. Each of these 2D blending processes is described by a 2D blending matrix, which has as many rows as there are crossline sources,  $N_{s_x}$ . (b) The 2D blending matrices are assembled in a single 3D blending matrix,  $\Gamma$ , which has  $N_{s_x}$  by  $N_{s_y}$  rows.

## 4-2 3D $f-k_x-k_y$ Filter

In section 2-2-3 the 2D  $f$ - $k$  filter was introduced. In 3D there are two spatial directions ( $x, y$ ), i.e. the filter can be extended to a 3D  $f$ - $k_x$ - $k_y$  filter.

For this purpose one considers a 3D common-receiver gather,  $\mathbf{p}(t, x_s, y_s)$ , and brings it to the  $f$ - $k_x$ - $k_y$  domain by applying a 3-dimensional Fourier transform. Next, a constant frequency slice is selected. This leaves a 2D matrix, which captures the crossline and inline wavenumbers ( $k_x, k_y$ ) as shown in Figure 4-4a. The minimum wavefield velocity,  $v_{min}$ , and the frequency,  $f$ , determine the maximum wavenumber,  $k_{max}$ , according to equation 2-7;

$$k_{max} = \frac{f}{v_{min}}. \quad (4-1)$$

The total wavenumber,  $k_T$ , must be smaller than the maximum wavenumber,  $k_{max}$ ,

$$k_T = \sqrt{k_x^2 + k_y^2} < k_{max}. \quad (4-2)$$

Hence the signal "cone" is defined by a circle (see Figure 4-4b). This is repeated for each frequency component, such that the overall  $f$ - $k_x$ - $k_y$  mask is a 3D cone (see Figure 4-4c). The cone can be sorted in a 2D view according to section 4-1 as illustrated in Figure 4-4d and Figure 4-4e. Finally, this mask is computed for each receiver gather.

For comparison, a 2D  $f$ - $k$  filter is designed for 3D data and plotted in a 2D view in Figure 4-5. Note that the 3D  $f$ - $k_x$ - $k_y$  filter (see Figure 4-4) removes significantly more incoherent energy than the 2D  $f$ - $k$  filter.

## 4-3 Results

The 3D  $f$ - $k_x$ - $k_y$  filter removes incoherent energy in the crossline and inline direction. The 3D blended acquisition design suggested in this thesis blends shots within the same crossline. Hence, an underlying question is whether an extension of the 2D  $f$ - $k_x$  filter to the inline direction provides significant deblending enhancements.

For this purpose the synthetic data of Figure 4-6a are blended: Within each crossline there are 21 sources, which are blended in 3 experiments. For each experiment 7 randomly selected sources are blended with random time delays, i.e. the blending pattern with mixed incoherency is applied. The maximum allowed firing-time delay is set to 400 ms. The incoherency measure of the used blending matrix,  $\Gamma$ , is  $\mu = 99\%$ .

The blended data are deblended with the 3D deblending algorithm. In one case a 2D  $f$ - $k_x$  filter is applied (see Figure 4-6c). In the other case a 3D  $f$ - $k_x$ - $k_y$  filter is applied (see Figure 4-6d). It is clearly visible that the deblending quality increases significantly with the 3D  $f$ - $k_x$ - $k_y$  filter. Figure 4-7 displays a 420 ms time slice of each subplot in Figure 4-6.

In order to quantify the quality gap between the results with 2D and 3D filters, the data of Figure 4-6a are blended with maximum firing-time delays varying between 40 ms and 400 ms. The blended data are deblended in one case with a 2D  $f$ - $k$  filter, and in the other case with a 3D  $f$ - $k_x$ - $k_y$  filter. The resulting quality factors are shown in Figure 4-8.

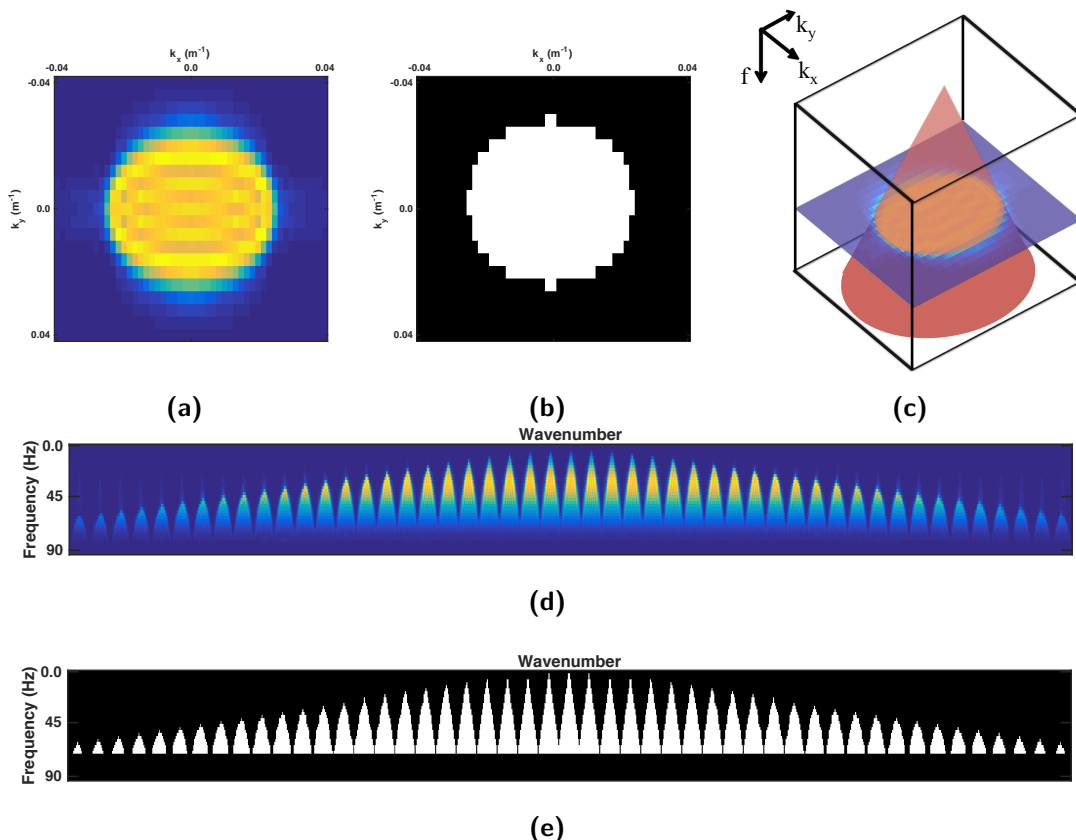


**Figure 4-4:** Illustration of the 3D  $f$ - $k_x$ - $k_y$  filter. (a) is a 40 Hz frequency slice of the  $f$ - $k_x$ - $k_y$  spectrum of the data in Figure 4-2.  $k_x$  and  $k_y$  refer to the crossline and inline wavenumber respectively. (b) is a 40 Hz frequency slice of the  $f$ - $k_x$ - $k_y$  mask, where the white area equals 1 and the black area is 0. (c) shows the 40 Hz frequency slice of (a) sorted in a 3D cube. The red cone represents the edge of the 3D  $f$ - $k_x$ - $k_y$  filter mask. (d) and (e) display the  $f$ - $k_x$ - $k_y$  data spectrum and mask sorted according to section 4-1, i.e. each sub-cone refers to one inline wavenumber. Note that due to the sorting the wavenumber axis is a mix of crossline and inline wavenumbers. For this reason the wavenumber axis has no labels.

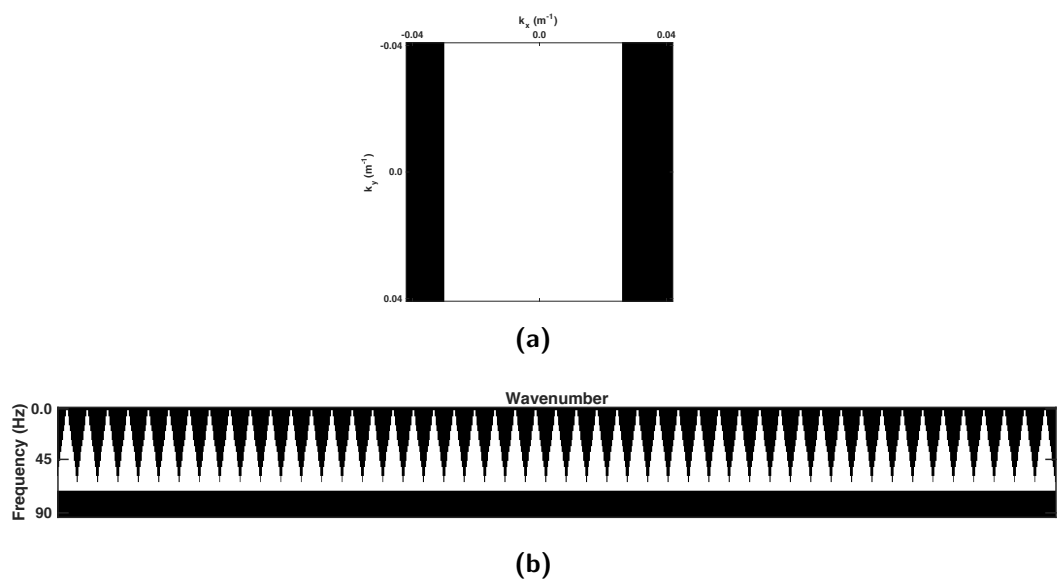


**Figure 4-5:** 2D  $f$ - $k_x$  filter for 3D data. (a) shows a 40 Hz frequency slice of the  $f$ - $k_x$ - $k_y$  spectrum, where the white area equals 1 and the black area is 0. Note that the filter is not affecting the inline wavenumbers  $k_y$ . (b) illustrates the 2D  $f$ - $k_x$  filter sorted according to section 4-1. Each cone represents a 2D  $f$ - $k$  filter for a single inline wavenumber.

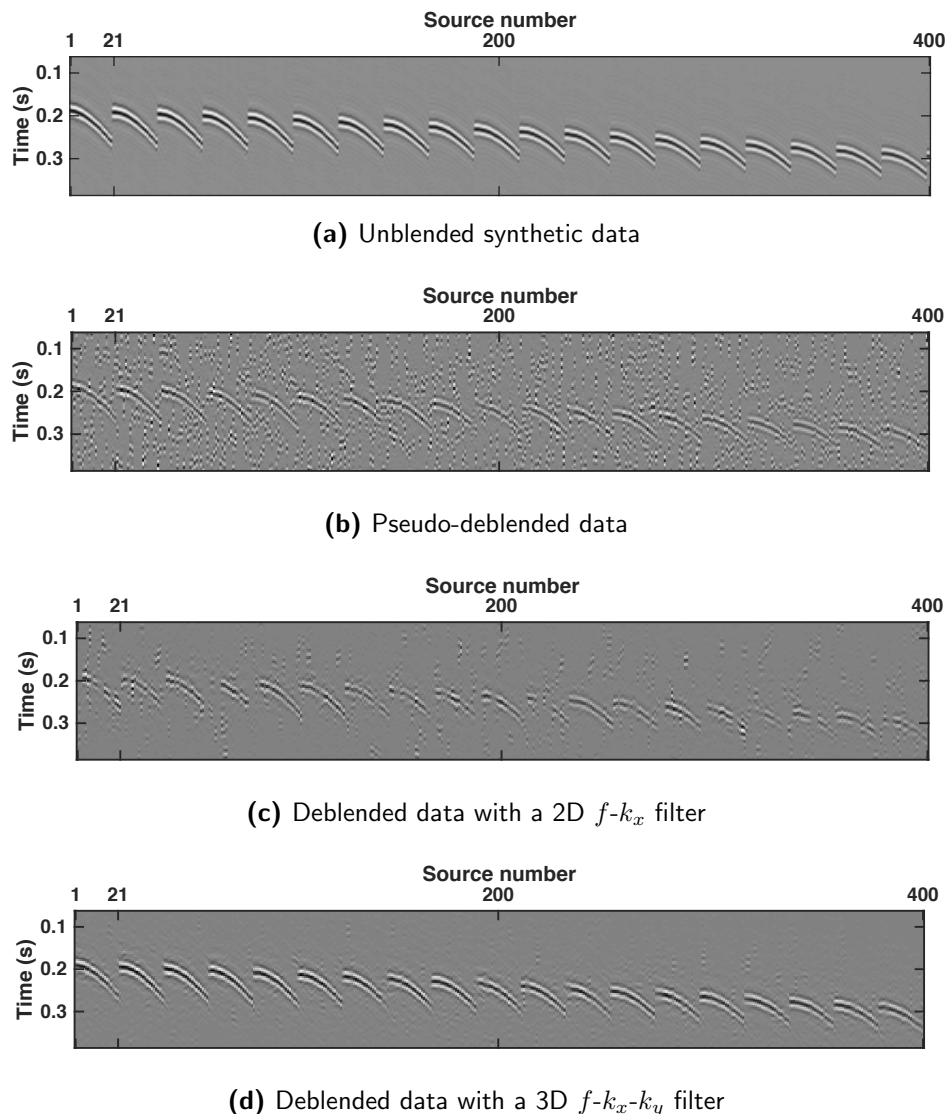


**Figure 4-6:** (a) is a synthetic 3D common-receiver gather in 2D view. The data are generated by 21 crossline shots and 51 inline shots. The shown section is a zoom on the strongest events. Figure 3-4a shows one crossline of the data for all times. The data are blended with a mixed incoherency blending pattern. Then, the 3D deblending algorithm is applied. (b) shows the pseudo-deblended data. In case (c) the algorithm uses a 2D  $f-k_x$  filter. In case (d) it uses a 3D  $f-k_x-k_y$  filter.

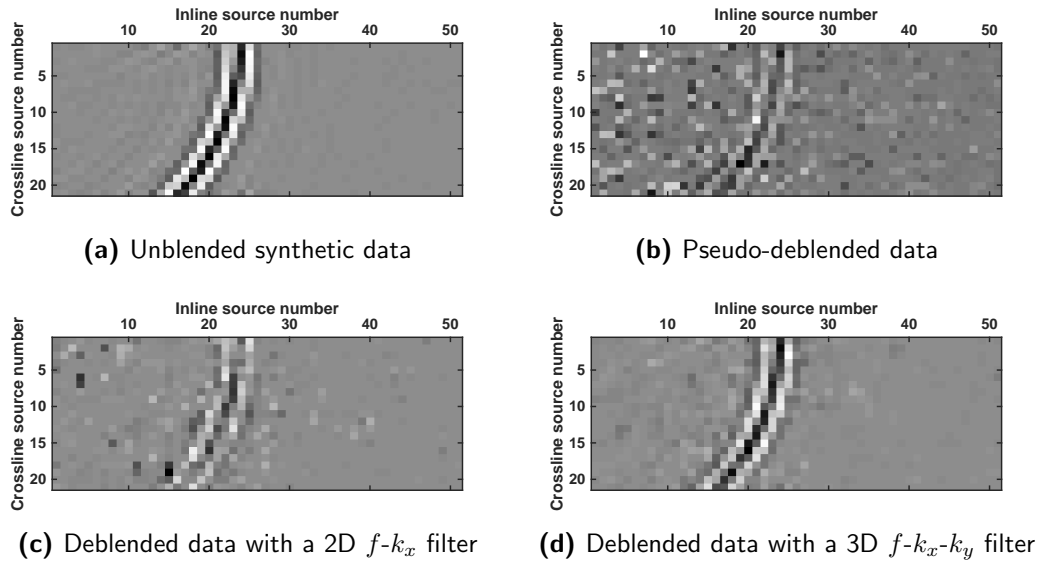


**Figure 4-7:** (a) - (d) show 420 ms time slices of the data in Figure 4-6.

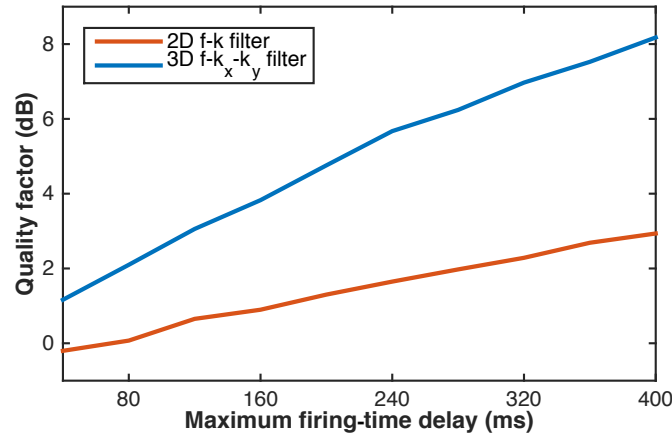


**Figure 4-8:** Comparison of the deblending quality with a 2D  $f-k_x$  filter and a 3D  $f-k_x-k_y$  filter. The data in Figure 4-6a are blended with varying maximum firing-time delay. Then the blended data are deblended using a 2D  $f-k_x$  filter and a 3D  $f-k_x-k_y$  filter.

#### 4-4 Conclusions

The presented deblending method uses a coherency constraint. It has been demonstrated that for 3D deblending the quality of the deblended data can be enhanced significantly by extending the coherency constraint to crossline direction too.



---

# Chapter 5

---

## Results Complex Synthetic Data

The chapters 3 and 4 demonstrated the importance of an incoherent blending pattern and introduced a 3D deblending method. In the following, the presented 3D deblending method is tested on 3D complex synthetic data using an optimized incoherent blending pattern. The test will be performed for the two acquisition designs proposed in chapter 1, *Large Crossline Source Array* and *Dense Crossline Source Array*.

### 5-1 Large Crossline Source Array

The *Large Crossline Source Array* was introduced in chapter 1 and is shown in Figure 5-1.

#### Source Grid Geometry

In this example, the data are acquired with a source grid of 21 sources along the crossline direction and 81 sources along the inline direction as depicted in Figure 5-2. The source spacing is 25 m in both directions and the receiver is placed in one corner of the source grid. The sources in Figure 5-2 are fired crossline-wise, i.e. first all sources of crossline 1 are fired, next, all sources of crossline 2, etc. In practice, the this data can be acquired as depicted by the moving vessel in Figure 5-2.

Note that for practical reasons in this thesis it is assumed that all crossline sources are fired at the same crossline position. Of course, this would not be true in marine acquisition because the sources constantly move such that the firing-time delay between successive shots causes a variation in the crossline shot position.

Gert Jan mentioned "Add irregular in discussion of chapter 6". What does he mean by this?

As might be clear from chapters 2 to 4 the deblending method is applied to individual common-receiver gathers. Thus, it is sufficient to proof that the method is capable to deblend a single common-receiver gather.

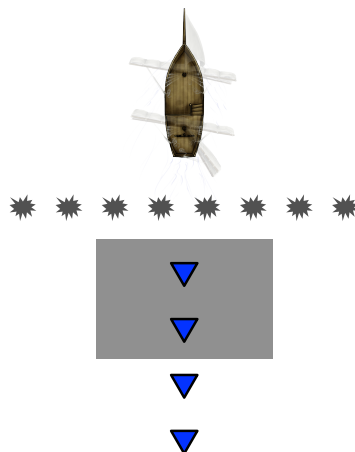


**Figure 5-1:** Large Crossline Source Array. The seismic sources are indicated in gray, and the receivers in blue. The gray rectangle illustrates the acquired area.

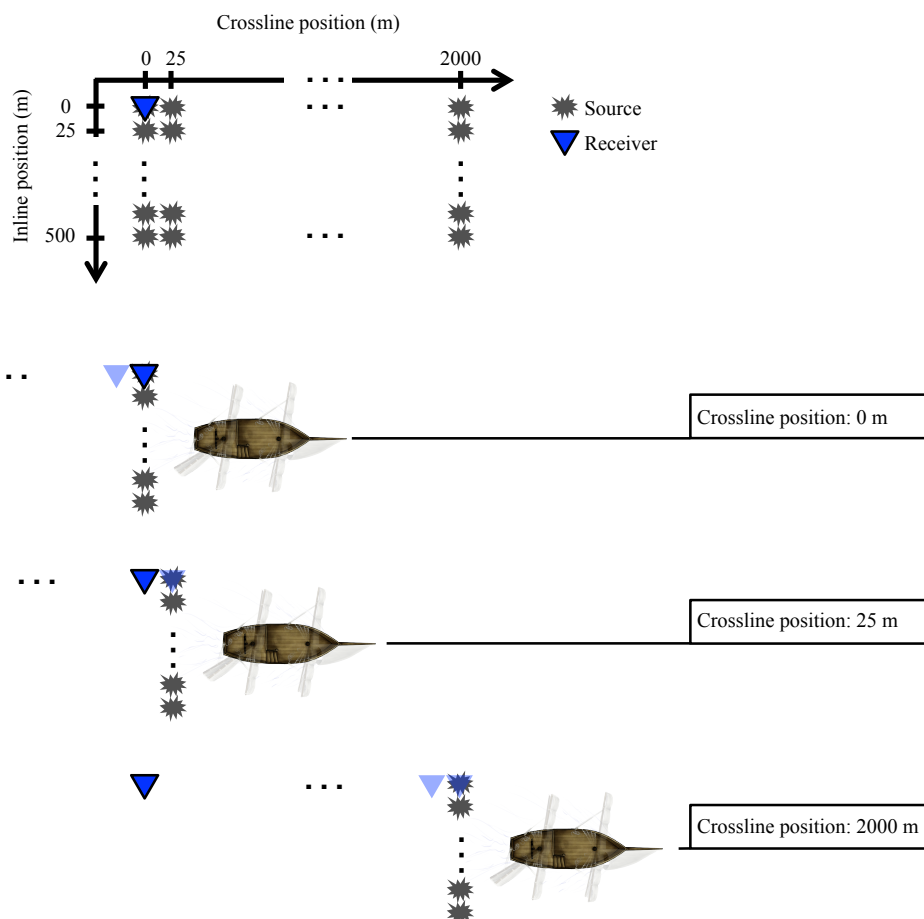


**Figure 5-2:** *Top:* Illustration of the source grid array. There are 81 sources along the inline direction and 21 sources along the crossline direction. For the *Large Crossline Source Array* the source spacing is 25 m in both crossline and inline direction.  
*Bottom:* The vessels show how the source grid can be built in practice.

## Blending

An unblended common-*shot* gather with the geometry of Figure 5-2 is extracted from an SEG SEAM data set. By applying reciprocity the common-shot gather is converted to a common-receiver gather. The crossline and inline spacings of the original SEAM data are both 50 m and the time sampling is 16 ms. The spacing and the time sampling are re-scaled to 25 m and 8 ms respectively, resulting in a new dataset with shallow water character. Figure 5-3a and 5-3e show an inline and crossline slice of the unblended data respectively. Time slices of the unblended data from 800 ms to 3.0 s are depicted in Figure 5-4 to 5-7.

The 21 shots within each crossline are blended in 3 experiments, i.e. there are 7 shots per experiment. Assuming that the seismic vessel moves with a speed of  $1.2 \text{ m s}^{-1}$ , it moves from one inline position to the next during 20.7 s, allowing for 6.9 s for each blended experiment. As the desired deblended trace length is 6.0 s the maximum firing-time delay is 900 ms.

Chapter 3 demonstrated that the optimal deblending result is achieved by maximizing the blending incoherency. Thus, a blending matrix,  $\Gamma$ , with maximum incoherency is created. The incoherency value is 99.65 %.

## Deblending Results

The unblended, pseudo-deblended and deblended data are shown in Figure 5-3 to 5-7. The deblended data have a quality factor of 14.2 dB.

Comparing the unblended and deblended inline slices in Figure 5-3a and 5-3c one observes that the strong events are almost perfectly deblended, e.g. the water bottom reflection and the strong overlapping events between 1.0 s and 2.0 s. Weak events such as the overlapping events between 2.0 s and 3.0 s are deblended well, but their continuity is distorted. The same applies to late events, as for example the hyperbolic event which starts at 3.0 s and 0.0 m offset.

The misfit between the unblended and deblended inline slice is illustrated in Figure 5-3d. In particular, in areas where several events intersect, e.g. between 1.5 s and 2.0 s, the misfit plot shows increased energy.

The crossline slices in Figure 5-3e to 5-3g confirm the observations of the inline slices. As there are only 21 sources in crossline direction a taper was applied to reduce artifacts caused by the Fourier transform. Thus, the events in the crossline slices are attenuated towards the edges.

The time slices of the unblended, pseudo-deblended and deblended data in Figure 5-4 to 5-7 confirm the different deblending performance for early versus late and weak events. The strong event in Figure 5-4 is deblended near to perfect. However, in Figure 5-5 some weak events at about 1600 m offset are hardly deblended. The strong events in Figure 5-6 and 5-7 are still deblended even though these time slices corresponds to a late time (1.8 s and 3.0 s).

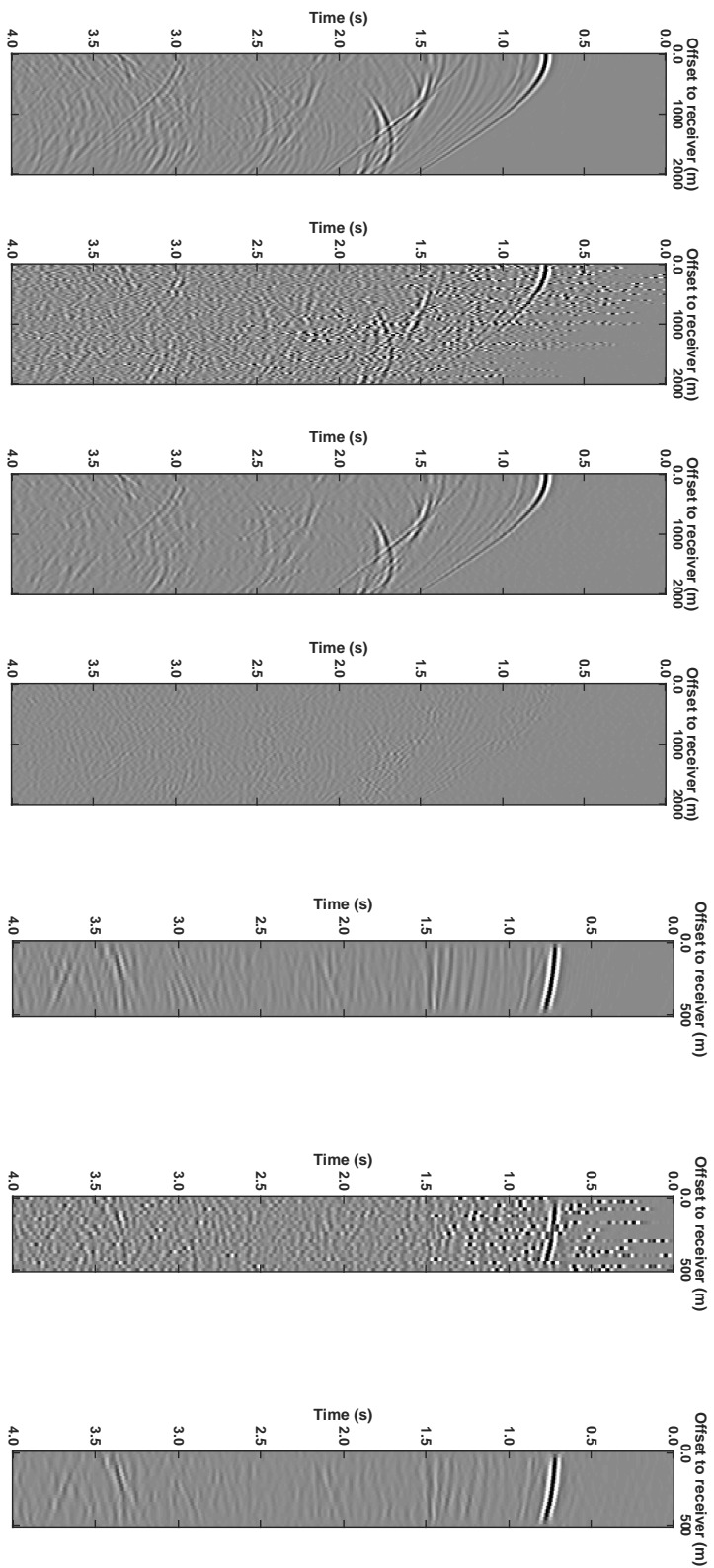


**Figure 5-3: Large Crossline Source Array**

(a)-(d) show an inline slice of the unblended, pseudo-deblended, deblended and misfit data respectively. (e)-(g) show a crossline slice of the unblended, pseudo-deblended and deblended data respectively. The shown seismic sections are common-receiver gathers. Note that for better visibility the crossline and inline offset axis do not have the same scale.

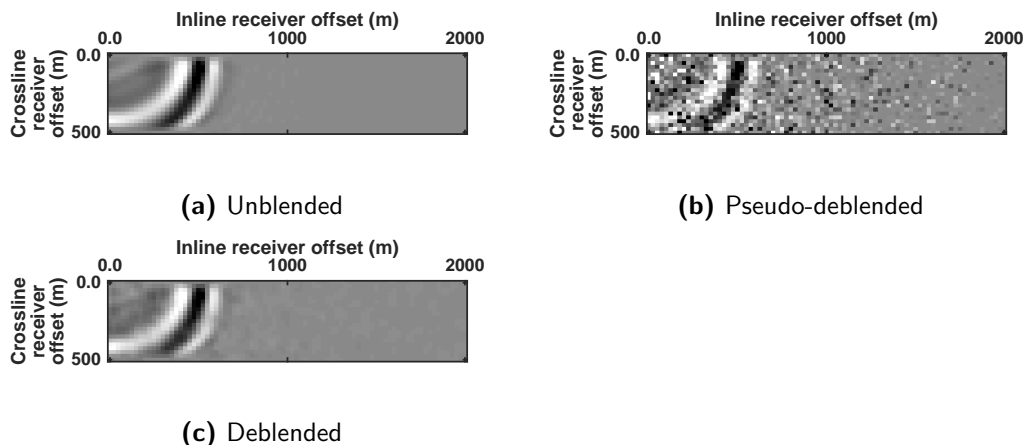


**Figure 5-4:** 800 ms time slice of the (a) unblended, (b) pseudo-deblended and (c) deblended data.

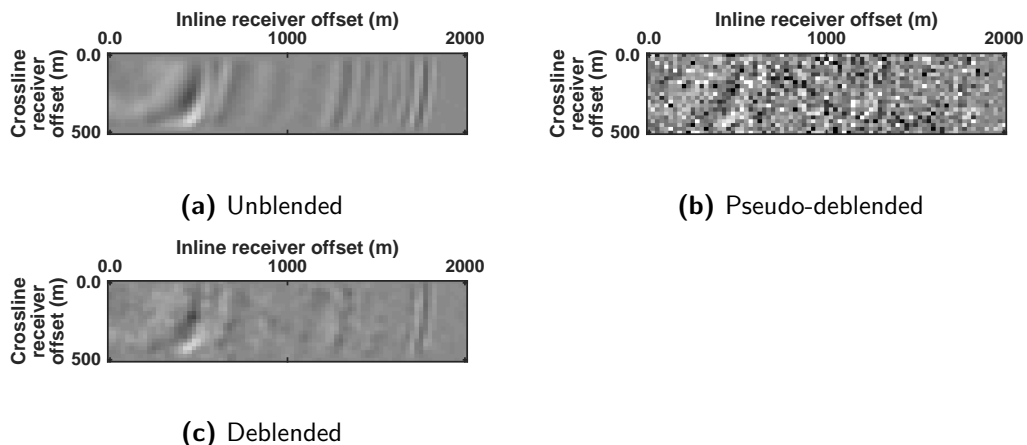


**Figure 5-5:** 1400 ms time slice of the (a) unblended, (b) pseudo-deblended and (c) deblended data.

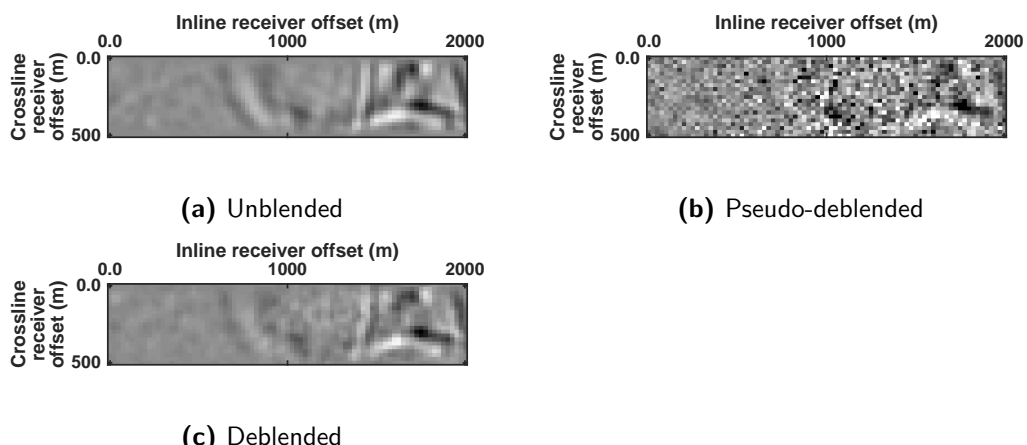


**Figure 5-6:** 1800 ms time slice of the (a) unblended, (b) pseudo-deblended and (c) deblended data.

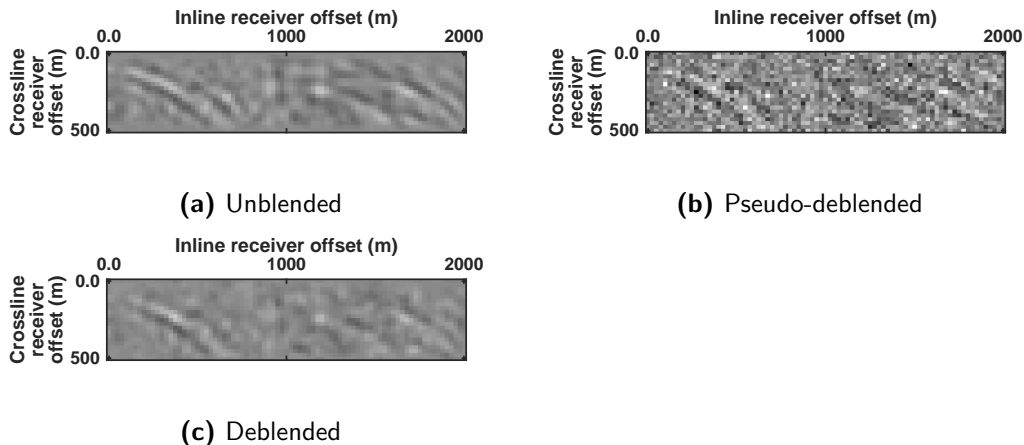


**Figure 5-7:** 3.0s time slice of the (a) unblended, (b) pseudo-deblended and (c) deblended data.

## 5-2 Dense Crossline Source Array

The *Dense Crossline Source Array* was introduced in chapter 1 and is shown in Figure 5-8.

The acquisition design is identical to the *Large Crossline Source Array* except that the source crossline-spacing is reduced to 12.5 m. The dense crossline-source spacing is obtained by interpolating the SEAM data in crossline direction via Fourier interpolation. Figure illustrates the acquisition set-up.

### Deblending Results

The deblending results for the *Dense Crossline Source Array* are achieved analogously to those of the *Large Crossline Source Array*. The deblended data have a quality factor of 20.8 dB, which is superior to the quality factor of the *Large Crossline Source Array* by 6.6 dB.

Comparing the unblended and deblended data in Figure 5-10 one observes that strong and early events are almost perfectly deblended. Besides, the late and weak events are also deblended well. Even weak intersecting events between 3.0 s and 3.5 s could be deblended.

The misfit plot in Figure 5-10d contains less energy than the one for the *Large Crossline Source Array* (see Figure 5-3d). However, some events of the data are visible in the misfit plot, e.g. the water bottom reflection. This means that during deblending the amplitudes were not perfectly recovered.

The time slices in Figure 5-11 to 5-14 confirm the good deblending performance. Note that the *Dense Crossline Source Array* performed better in deblending weak and late events than the *Large Crossline Source Array*. For example, the *Dense Crossline Source Array* succeeds in deblending the weak events in Figure 5-12 at an offset of about 1600 m, whereas the *Large Crossline Source Array* was not capable to deblend all of them (see Figure 5-5).

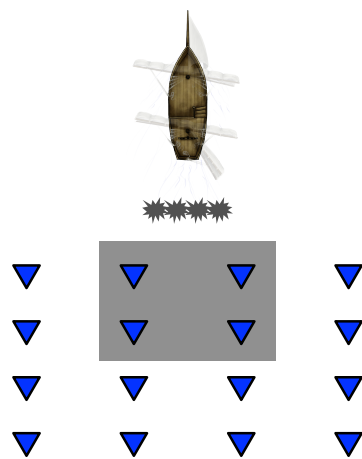


**Figure 5-8:** Dense Crossline Source Array. The seismic sources are indicated in gray, and the receivers in blue. The gray rectangle illustrates the acquired area.

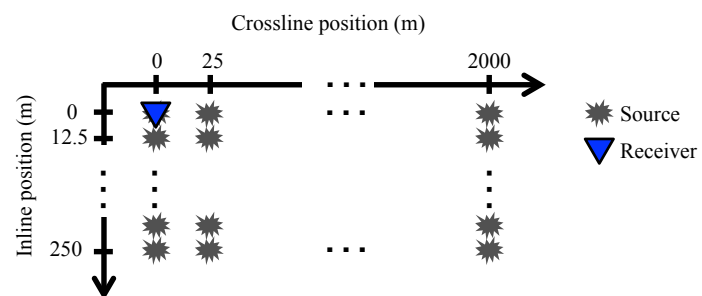


**Figure 5-9:** Illustration of the source grid array for a *Dense Crossline Source Array*.

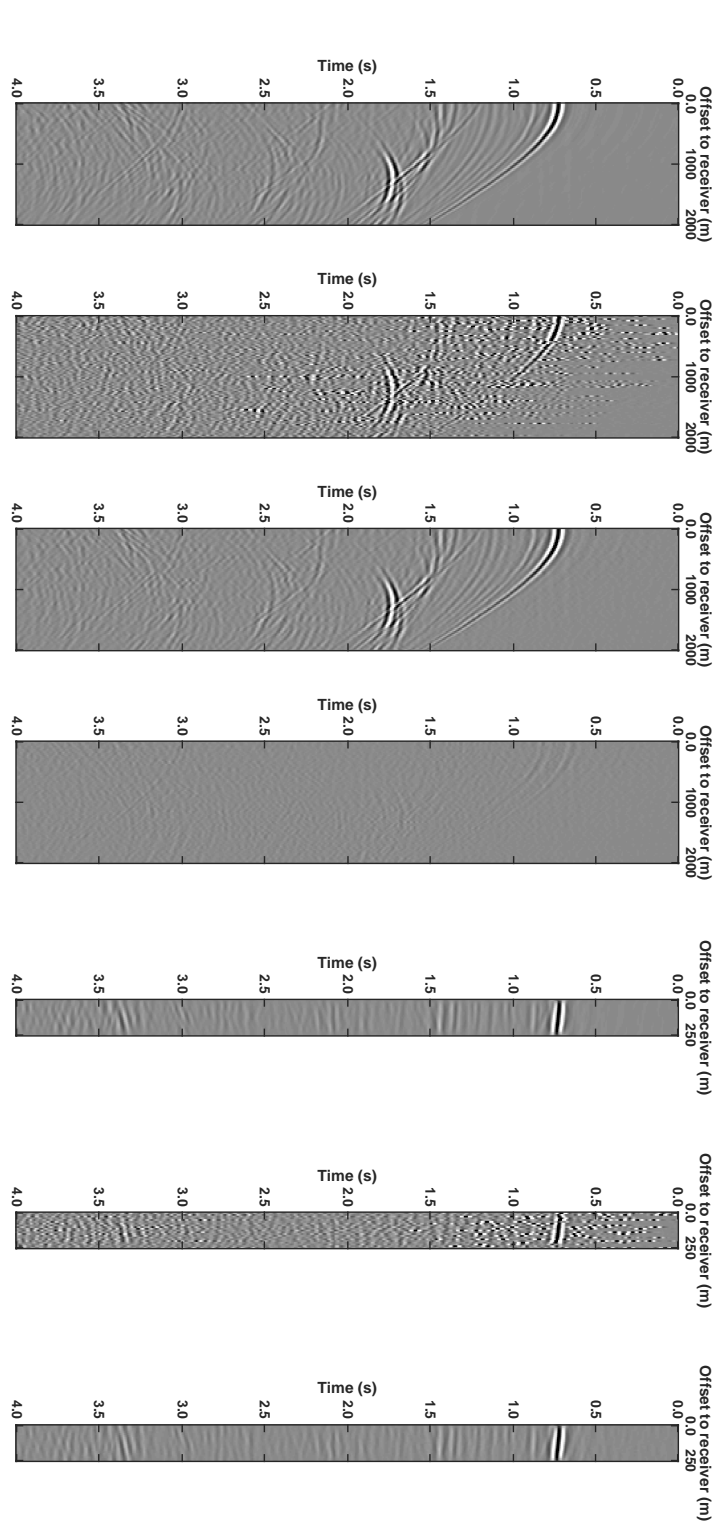


**Figure 5-10: Dense Crossline Source Array**

(a)-(d) show an inline slice of the unblended, pseudo-deblended, deblended and misfit data respectively. (e)-(g) show a crossline slice of the unblended, pseudo-deblended and deblended data respectively. The shown seismic sections are common-receiver gathers. Note that for better visibility the crossline and inline offset axis do not have the same scale.

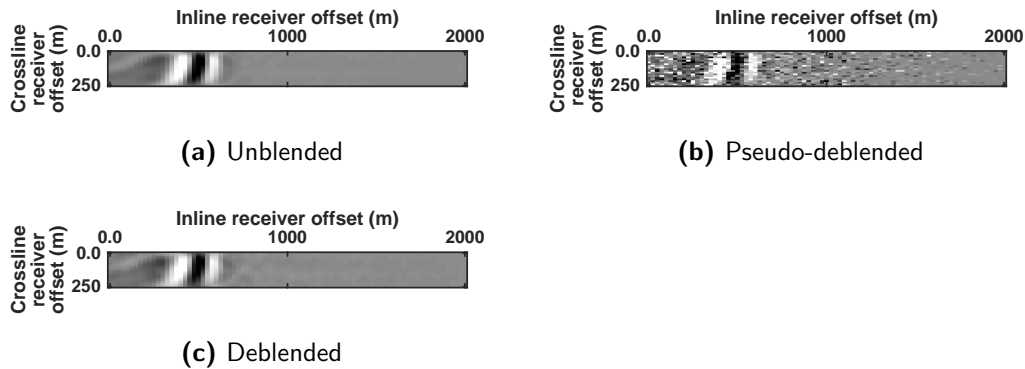


**Figure 5-11:** 800 ms time slice of the (a) unblended, (b) pseudo-deblended and (c) deblended data.

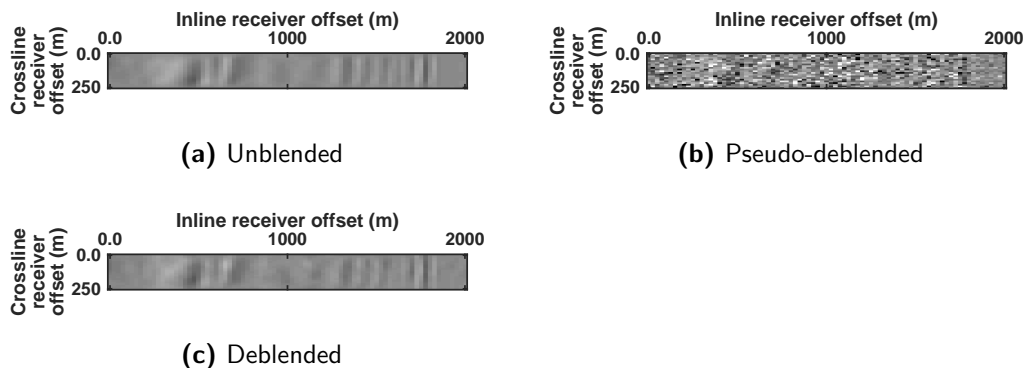


**Figure 5-12:** 1400 ms time slice of the (a) unblended, (b) pseudo-deblended and (c) deblended data.

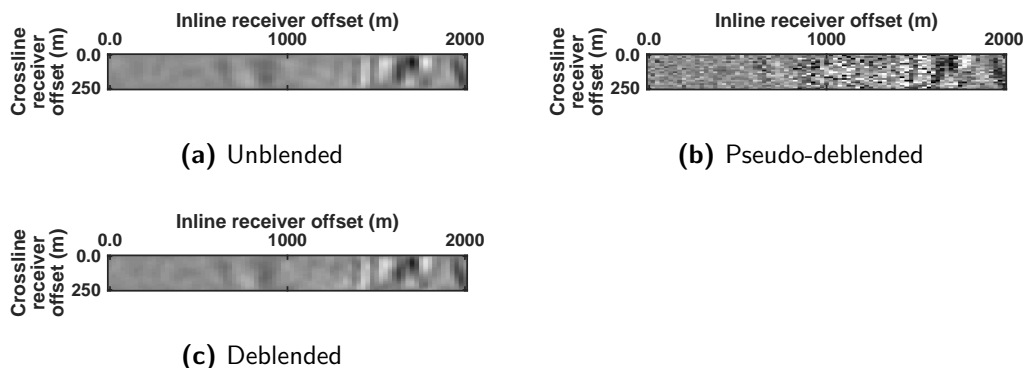


**Figure 5-13:** 1800 ms time slice of the (a) unblended, (b) pseudo-deblended and (c) deblended data.

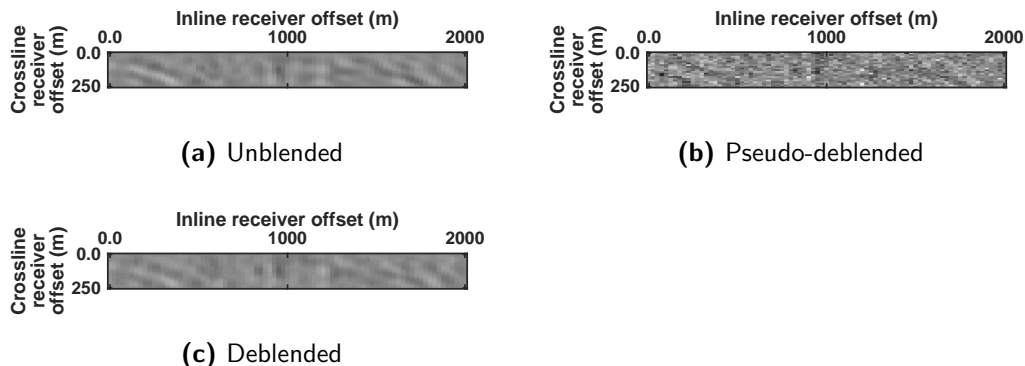


**Figure 5-14:** 3.0 s time slice of the (a) unblended, (b) pseudo-deblended and (c) deblended data.

### **5-3 Conclusion and Discussion**

The complex synthetic data example demonstrates the feasibility of 3D crossline blending and deblending. Both acquisition designs deblended strong and early events near to perfect. Weak and late events in the deblended *Large Crossline Source Array* are less continuous as their unblended version. The *Dense Crossline Source Array* managed to deblend these weak and late events very well. As in practice especially the late events are of interest the deblending performance is satisfying.

The *Large Crossline Source Array* covers an area twice as large as the *Dense Crossline Source Array*. The advantage of the *Dense Crossline Source Array* is that it provides higher deblending quality than the *Large Crossline Source Array*, in this example the deblending quality differs by 6.6 dB.

Note that the direct wave has been removed before blending because it has a significantly stronger amplitude than the other events. In practice, one has to remove the direct waves present in the data in a separate processing step.

---

# Chapter 6

---

## Conclusions and Discussion

### 6-1 Conclusions

The main conclusions of this thesis are:

- The feasibility of the proposed 3D blended acquisition was validated by deblending a complex synthetic dataset. The key elements of successful 3D deblending were found to be maximizing the incoherency of the blending pattern, and applying a 3D deblending method.
- The deblending success is very sensitive to the blended acquisition design. The blending noise, or source interference, should be as incoherent as possible. This incoherency can be generated by random firing-time delays and by permuting the shot positions randomly. This can be expressed by an incoherency measure. In addition, the maximum firing-time delay has to be designed in order to adjust the deblending quality.
- This thesis presented a 3D deblending method, which takes advantage of a coherency constraint of the data in the  $f-k_x-k_y$  domain, in contrast to 2D deblending methods, which only use coherency constraints in the  $f-k_x$  domain. It was demonstrated that the 3D method results in significantly better deblending quality than the 2D method.

### 6-2 Discussion

The presented deblending method is performed in the common-receiver domain. Thus, a dense spatial source sampling is required. If we were not restricted to a dense spatial source sampling we could design more incoherent blending patterns. In future work one should try to overcome this restriction e.g. by interpolating "missing" sources.

This thesis demonstrated that the blended acquisition should be as incoherent as possible to achieve optimal deblending results. Thus, one should investigate further possibilities to

generate incoherent blending noise. Incoherency can be increased by adding further degrees of freedom to the blending pattern. For example, the amplitudes of the blended shots can be varied randomly, several source vessels can be used in order to achieve more freedom for the random shot position permutation, or one can allow shot repetition as proposed by Wu (2014).

In this thesis it was assumed that the vessel stops at each crossline shot position until all crossline sources are fired and recorded. For a practical realization the continuous vessel movement must be taken into account. This movement will increase the variation of the shot positions. Consequently, this correction is promising to increase the degree of incoherency further, which enhances the deblending quality.

Chapter 5 tested the presented 3D deblending method on two acquisition designs, *Large Crossline Source Array* and *Dense Crossline Source Array*. Of course, other acquisition designs can be realized under the condition that the spatial source sampling is sufficiently dense and that the blending pattern is sufficiently incoherent.

Currently, crossline sources are not used in seismic acquisition. Unblended crossline sources are very unpractical because the required time separation between successive shots results in coarse spatial source sampling. However, this problem can be overcome by blending the crossline sources. The synthetic data examples demonstrate that 3D crossline blending has potential to enhance seismic acquisition. From today's point of view 3D crossline blending is not sufficiently developed to be realized on an industry scale. However, in view of increasing challenges in seismic acquisition new approaches such as 3D crossline blending are required and promising to gain significant interest in the future.

Add

In practice, densely-spaced crossline sources can be difficult to control, e.g. non linear effects start to occur. By introducing a second receiver, and by restructuring the geometry unit according to Figure ?? the crossline spacing can be doubled while the acquired common-depth points (CDPs) remain. Thus, if the 3D deblending method succeeds in deblending the acquisition geometry in Figure ?? it is also capable to deblend the equivalent geometry unit in Figure ??.

---

# Acknowledgements

Thanks to my colleagues Gert-Jan, Rolf and Martijn for the great table soccer competitions, which were very inspiring for my thesis. In particular, the concept of incoherent shooting was shaped significantly during these legendary matches.

Delft, University of Technology  
August 3, 2015

Christian Reinicke Urruticoechea



---

## Bibliography

- Beasley, C. J., Chambers, R. E., Jiang, Z., et al. (1998). A new look at simultaneous sources. In *SEG Technical Program Expanded Abstracts*, volume 17, pages 133–135.
- Berkhout, A. (1982). *Seismic Migration: Imaging of Acoustic Energy by Wave Field Extrapolation, Part A: Theoretical Aspects*. Elsevier.
- Ibrahim, A. and Sacchi, M. D. (2013). Simultaneous source separation via robust time variant radon operators.
- Ibrahim, A. and Sacchi, M. D. (2015). Fast simultaneous seismic source separation using stolt migration and demigration operators. *researchgate.net*.
- Mahdad, A., Doulgeris, P., and Blacquiere, G. (2011). Separation of blended data by iterative estimation and subtraction of blending interference noise. *Geophysics*, 76(3):Q9–Q17.
- Vaage, S. T. (2002). Method and system for acquiring marine seismic data using multiple seismic sources. US Patent 6,906,981.
- van Dedem, E. J. (2002). *3D surface-related multiple prediction*. PhD thesis, TU Delft.
- van Groenestijn, G. J. A. (2010). *Estimation of Primaries and Multiples by Sparse Inversion*. PhD thesis, TU Delft.
- WEC, W. E. C. (2013). World energy resources.
- Wikigrewal (2015). <http://wikigrewal.com/what-is-a-offshore-seismic-survey-vessel/>.
- Womack, J., Cruz, J., Rigdon, H., and Hoover, G. (1990). Encoding techniques for multiple source point seismic data acquisition. *Geophysics*, 55(10):1389–1396.
- Wu, S. (2014). Seismic deblending by shot repetition. Master's thesis, TU Delft.



---

## Appendix A

---

# The back of the thesis

### A-1 An appendix section

List of matlab functions!

#### A-1-1 An appendix subsection with C++ Listing

```
//  
// C++ Listing Test  
//  
#include <stdio.h>  
for( int i=0;i<10;i++ )  
{  
    cout << "Ok\n";  
}
```

1

6

#### A-1-2 A Matlab Listing

```
%  
% Comment  
%  
n=10;  
for i=1:n  
    disp('Ok');  
end
```

5